Model Implementation and Verification of the Envelope, HVAC and Controller of an Office Building in Modelica: Supplementary Material

Nomenclature

Acronyms and codes

BES	Building Energy Simulation
BF	Borefield
BMS	Building Management system
CAV	Constant Air Volume
CCA	Concrete Core Activation
CH	Chiller
CWST	Chilled Water Storage Tank
DHW	Domestic Hot Water
HC	Heating Coil
HEX	Heat Exchanger
HP	Heat Pump
HVAC	Heating, Ventilation and Air Conditioning
HWST	Hot Water Storage Tank
IEH	Indirect Evaporative Heat Exchanger
IT	Cooling Data Center
LMTD	Logarithmic Mean Temperature Difference
MPC	Model Predictive Control
PEL	Pellet Furnace
RAD	Radiator
RES	Renewable Energy Sources
RMAOT	Running Mean Average Outdoor Temperature
SD	Slot Diffuser
SOL	Solar Collector
TABS	Thermally Activated Building Systems
UFAD	Underfloor Air Distribution
VAV	Variable Air Volume

Indices

amb	Ambient
b	Borefield
bs	Building shade
c	CCA collector
col	Collector
con	Convective
dif	Diffuse
dir	Direct
eas	East
flo	Floor
g	Gap between shading and window
gro	Ground
h	Hot water storage tank
HP	Heat pump
I	Integrator
in	Inlet
inf	Infiltration
int	Interior
lw	Longwave
nom	Nominal
ov	Overhang
plm	Thermal plume
pro	Production
rad	Radiator
req	Required
ret	Return
s	Solar collector
set	Set point
sf	Side fin
sou	South
sup	Supply
sw	Shortwave
th	Threshold
ver	Vertical
wes	West
win	Window

Symbols

$\dot{m}$	Mass flow rate
$\dot{Q}$	Heat flow rate
$\dot{V}$	Volumetric flow rate
ϵ	Emissivity
ϕ	Azimuth angle
ρ	Density
τ	Time constant
ACH	Air changes per hour
alt	Solar altitude angle
aw	Anti-windup
lat	Latitude
lon	Longitude
mod	Modulation fraction
NTU	Number of transfer units
θ	Tilt angle
A	Surface area
C	Heat capacity rate
c_m	Scaling factor for thermal mass
c_p	Specific heat capacity
d	Depth of shading
g	G-value of glazing
H	Solar irradiance
h	Convective heat transfer coefficient
I	Integer variable
I	Integral value
k	Flow coefficient
k	Thermal conductivity
K_v	Flow coefficient
L	Length
n	Pump speed
P	Active electrical power
p	Pressure
s	Status variable: on or off
T	Dry bulb temperature
t	Time

U	Thermal conductance	V	Volume
u	Input signal	y	Control signal or output signal

1 Introduction

This document contains the description of an office building and its model implementation together with some verification results. Firstly, relevant technical parameters, data sheets and building plans are included. Secondly, important model implementations and equations are presented or referenced. Finally, some model verifications are discussed.

This document is supplementary material to the article entitled "*Model Implementation and Verification of the Envelope, HVAC and Controller of an Office Building in Modelica*" and therefore mostly contains complementary information that could not be included in the paper.

2 Building Description

The office building, named Solarwind, is located at $11 - 13$ rue de l'industrie, 8399 Windhof, Luxembourg. It consists of six floors above ground and of three more underground floors that contain Heating Ventilation and Air Conditioning (HVAC) equipment and parking space. The building was designed to be an examplary showcase towards the Luxembourg and European design and construction industry of a holistic and integrated operation and design sustainability approach for future oriented office buildings. It is an initiative of 'In der Laey', with PROgroup (project management and environmental assessors) and Schuler (project developer) as building owners and opened in November 2012.

The approach was driven by the 4 P philosophy: 1) Integration of dedicated water-, waste- and cradle to cradle management, minimal energy use starting from a passive building envelope, maximizing renewable energy by simulation based evaluation in the design phase. (Planet) 2) Providing state of the art comfort such as indoor environmental quality and services for the tenants. (People) 3) Setting an economically feasible example, reducing costs and improving productivity. (Profit) 4) Visibly sharing the building technologies and operation experiences, integrating a conference centre, creating an educational tour for schools as well as for other visitors, and partnering with relevant research. (Pedagogy, French for education)

A triple certified environmental impact assessment (BREEAM, HQE, DGNB) has been carried out to ensure the low impact targets set for the lifecycle of the Solarwind building. The behaviour of the building (energy use, control, comfort) has been fine tuned during the first years of operation and has been followed up since then.

The building envelope, HVAC, control strategy and measurement data are now discussed. This description is intended to be self-contained and may therefore contain information that also appears in the article.

2.1 Building Envelope

Solarwind is an L-shaped office building that consists of six conditioned floors. Figure 1 shows an aerial picture of the building and its immediate surroundings.

The four middle floors have a very similar geometry and are denoted using numbers 0 through 3. The floor plan of floor 0 is included in Figure 2. These floors consist of offices and furthermore contain two stairways and two restrooms. The area around the building is subsided relative to street level such that floor -1 is also visible in Figure 1. Floor -1 consists of a creche, a restaurant, a gym, offices, stairways, restrooms and a room for waste disposal. Floor 4 has only one third of the surface area of the other floors and is located centrally on the roof of floor 3. It consists of 8 meeting rooms and is surrounded by a green roof, solar thermal collectors, a terrace and technical rooms containing HVAC equipment. Solarwind is situated at the edge of an industrial park. The short leg of the 'L' points

Figure 1: Aerial photograph of Solarwind and its surroundings. The PV panel shading on the south façade, green roof, green façade and solar thermal collectors are clearly visible. At the east façade one of the boxes is visible. Courtesy of PROgroup.

south-west, at an angle of 27 degrees relative to south. The east façade is shaded by a parallel building at a distance of 16 m and with a height of about 9.2 m [1]. The south façade has limited shading by a building at a distance of about 50 m. The west and north façades have little shading since they are surrounded by farmland and low growing bushes or trees.

The building structure consists of 25 cm thick concrete floors that are supported by concrete columns. The region around the stairways, restrooms and elevators contains walls of solid concrete that also provide structural support. Zone separating walls consist mostly of solid concrete, or of 14 cm thick concrete blocks with a gypsum finish. Zones are usually further separated into individual rooms using light walls that consist of 10 cm of insulation material and 1.25 cm of plasterboard. The main façade is suspended from the concrete slabs. It consists of a wooden skeleton that is inflated with wood fibre (40 cm). The interior finish consists of plasterboard. The total wall thickness is 51 cm and its combined U value is 0.08 W/m^{2}K. Floor -1 and floor 4 have other wall types, including cellular concrete and insulated concrete walls. Schüco AWS 90.SI$^+$ frames with a U$_f$-value of 1.0 W/m^{2}K are used containing one of multiple triple glazing types with U$_g$ values of 0.5 W/m^{2}K or 0.6 W/m^{2}K. The glazing systems consist of clear glazing sheets of various thicknesses. A small number of windows is laminated. The two outer sheets are coated using coatings, among them: Guardian SunGuard Top Selective 60/28, Guardian Climaguard Premium, Guardian Sunguard HS SuperNeutral 62/34 and Glas Fandel Termo-Bit Premium. The glazing systems use an argon filling with 10 % air. The north façade has glazing with a g-value of 30.7 % and no further solar shading. The other façades have glazing with a g-value of 49.4 % and one of two types of solar shading. Photovoltaic solar panel overhangs provide passive shading on the south façade. Controllable exterior screens shade the east and the west façades. At the east and west sides of the building floors 1, 2 and 3 have one box that protrudes from the building. The box is 1.3 m deep and 5.45 m wide, and contains a window with a width of 2.5 m. The north side of floors 1, 2 and 3 each have two glazed boxes, of 2.9 m deep and 5 m wide, that protrude from the building. Its concrete floor and ceiling are insulated using 25 cm of insulation. The floor plate of floor -1 is insulated with 17.5 cm of insulation. The 29 cm thick concrete ceiling of floor 3 is insulated with 41 cm of insulation. Only floors 0 – 3 are modelled in the main model. Additionally, a model including floor -1 is included in one of the verifications. Floor 4 consists of meeting rooms and is not modelled.

2.2 Heating, Ventilation and Air Conditioning

Solarwind has following heat sources: four geothermal heat pumps, solar collectors and a pellet furnace. Outdoor air and the borefield can be used for passive cooling. A chiller is used for active cooling of a data center. These heat and cold sources are coupled to CCA slabs, heating coils, radiators, chilled ceilings, VAVs, and domestic hot water tanks. Furthermore, various pumps, pipes, valves, heat exchangers and storage tanks are used.

Tables 1 – 3 summarise what HVAC equipment is used for each floor, what their design sizes are and what connections exist between the components of the HVAC equipment. Moreover these tables summarize what parts of the building and HVAC are not modelled. More specifically, all components related to the chilled water circuit are not modelled since they are only used to cool the building data center, which is not of interest for our research. Figure 3 shows the hydronic systems of Solarwind, design sizes and temperatures and types of important valves and pumps. Further details are provided below.

Floors 0 – 3 are each cooled or heated using both a ventilation system and Concrete Core Activation (CCA). The CCA consists of concrete slabs with a thickness of 25 cm or 29 cm and Uponor Contec modules of various sizes that are embedded in the middle of the slab. The modules consist of 20 × 2.3 mm PE tubes with a core to core spacing of 15 cm. The CCA supply temperature of the north and south parts of the building are each controlled individually using three-way valves. A pump with

---

[1]Surrounding building height and distances are estimated based on satellite images from Google maps. The shade cast by surrounding building was compared to the shade cast by Solarwind. Using the known height of Solarwind, the height of the other building was computed.
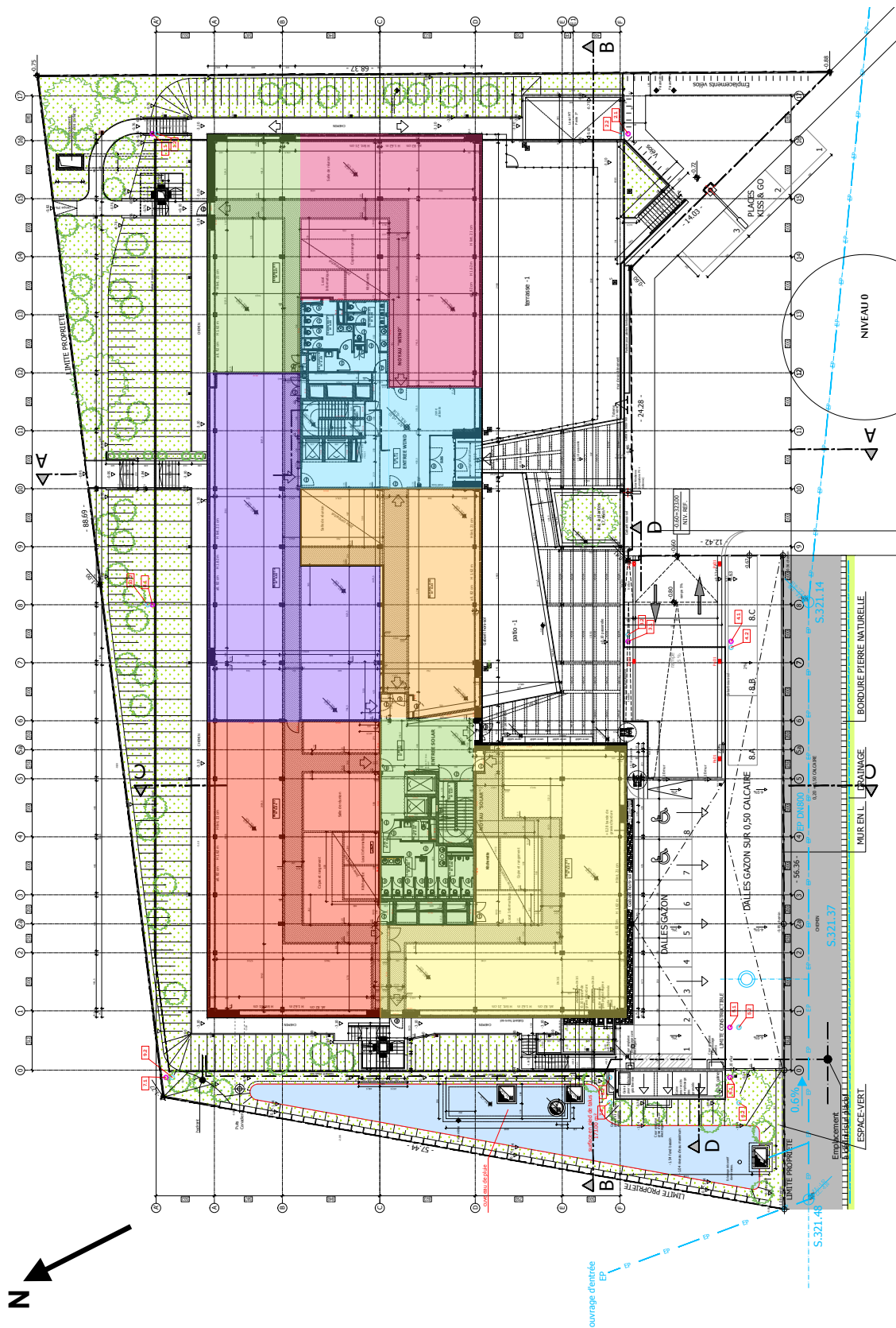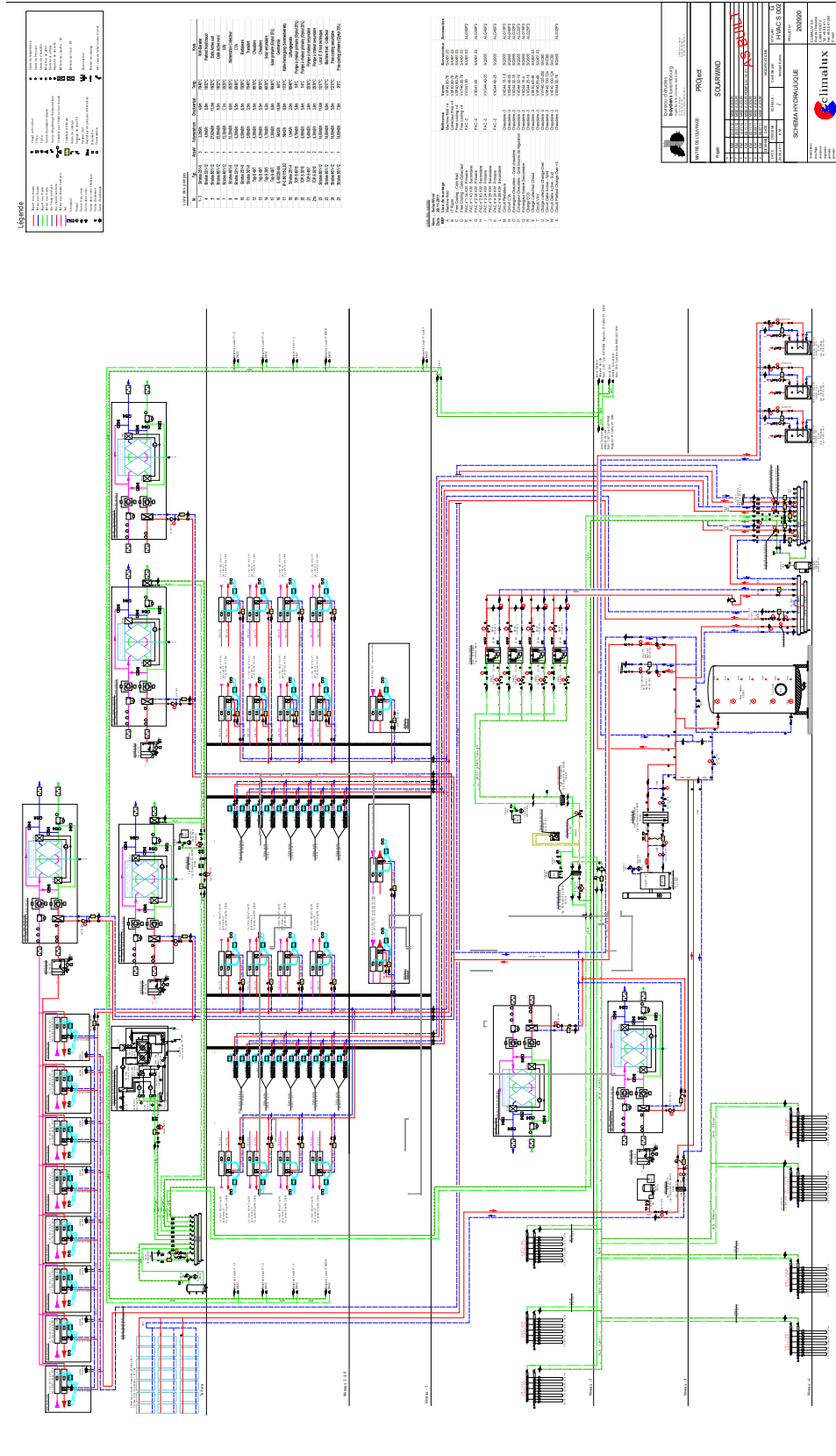
Figure 2: Ground plan of floor 0 with zones indicated in color. Courtesy of Boydens engineering, Architecture Dariusz Pawlowski

5

Figure 3: Hydraulic plan of HVAC equipment

6

a fixed head of 12 m supplies pressure to the two CCA circuits. The mass flow rates of each of the three north and the three south oriented zones of each floor are controlled individually using two-way valves. Nominal flow rates are in the order of 10 $\text{kgh}^{-1}\text{m}^{-2}$. The two CCA circuits and the chilled ceiling circuit of floor 4 are connected to a central collector that is either supplied by chilled water from the borefield (passive cooling) or warm water from the heat pumps.

Passive cooling is supplied using a geothermal borefield that consists of 99 boreholes. 22 boreholes are located next to the building and have a depth of 39 m. The remaining 77 boreholes are located underneath the building and have a depth of 27 m. The borehole radius is 15 cm and PE100 double U tubes with a diameter of 2.5 cm and a thickness of 2.3 mm are used.

Four Viessmann geothermal heat pumps supply heat to the CCA and VAV heating coils. Two have a nominal thermal power of 29 kW. The two others have a nominal thermal power of 45 kW. The heat pumps draw heat from the borefield and the chilled water system.

Supply air enters the building through a ducted underfloor air distribution system, which is connected to the main ventilation shafts in the center of the east and the west wings of the building. Return air leaves the zone through vents in each zone corridor. The supply and return air flow rates of each zone are controlled using 1, 2 or 3 individually controlled sets of Variable Air Volume (VAV) units. The VAVs have a nominal flow rate of 900 m^3h^{-1}. The control knobs on the unit are configured such that the lower and upper bounds of the flow rate are 30 % and 65 %, such that the effective nominal flow rate is 580 m^3h^{-1} per VAV. Each supply VAV has a Heating Coil (HC) that uses heat from the heat pumps. Its flow rate is controlled using Siemens VDN115 valves. The west and east wings of floors $0 - 3$ each have a dedicated Menerga Adsolair type 58 Air Handling Unit (AHU) that each supply and extract air to or from six VAVs per floor through the main supply and a return air duct. Moreover, air is extracted from the restrooms in the east and west wing using Trox VSR 125 Constant Air Volume (CAV) units with nominal flow rates of 150 m^3h^{-1}. The heat recovering AHUs can cool passively using a bypass, or cool actively using an Indirect Evaporative Heat exchanger (IEH), or a modulating chiller. The AHU supply air is heated using a heating coil that uses hot water from a Hot Water Storage Tank (HWST) of 20 m^3. During winter a second heating coil can pre-heat the outdoor air that enters the AHU, which extracts heat from a data center.

Hot water for the stratified HWST is produced using 62 m^2 of solar collectors or using a wood pellet furnace of 100 kW. Cooler water from the tank bottom first passes through the solar collector circuit if it is enabled, which heats up the water, and then passes the through pellet furnace, which can heat the water further or serves as a backup during winter. A Belimo R240P-164 pressure-independent valve, which is not indicated in Figure 3, is used to control the flow rate through pump 11, which controls the flow rate of the circuit that connects the HWST, the solar collectors and the pellet furnace.

Hot water is further used to charge three Domestic Hot Water (DHW) storage tanks of 0.5 m^3 with an internal heat exchanger. Water from these three tanks is available in the building through circulation pipes.

2.3   Building Control

The building HVAC systems are controlled using SBC PCD3 programmable controllers that are interfaced through BACnet to a central Building Management System (BMS) developed by DRC. The BMS is used to change control set points and other parameters. These changes are logged but the logs are unavailable to the authors of this text.

The BMS considers subcircuits to which a *mode* is associated. Building measurements, outdoor measurements and the modes of other subsystems determine what mode is active. The active mode determines what parts of low-level controllers are activated and how their set-points are computed and tracked. The controllers include low-level PI(D) controllers, heating curves, delays, flip flops, hysteresis controllers and boolean logic, but also more advanced, proprietary algorithms or rules such as the on-off control sequence of the heat pumps.

This section describes only the parts of the control strategy that were modelled. The control

Table 1: Summary of main floor properties. Used symbols and codes are defined in Table 2 and Table 3 and in the nomenclature.

Floor	Main function	Surface area	AHU	Terminal unit	Cooling	Heating	Modelled
4	Meeting rooms	623 m²	5	VAV - HC - SD	CC	CC	no
3	Offices	2151 m²	1;2	VAV - HC - UFAD	CCA1 + CCA2	CCA1 + CCA2	yes
2	Offices	2151 m²	1;2	VAV - HC - UFAD	CCA1 + CCA2	CCA1 + CCA2	yes
1	Offices	2151 m²	1;2	VAV - HC - UFAD	CCA1 + CCA2	CCA1 + CCA2	yes
0	Offices	2151 m²	1;2;7	VAV - HC - UFAD	CCA1 + CCA2	CCA1 + CCA2	yes
-1	Offices, gym, creche, restaurant	2091 m²	3;4;6	VAV - HC	CCA1 + CCA2	CCA1 + CCA2	no

Table 2: Summary of air handling unit types, nominal properties and configuration. Unmodelled AHU *components* are indicated using *

AHU	Type	Nom. flow rate	IEH	Chiller	Heating coils - heat source	Humidifier	Air source	Modelled
1	Adsolair 58 19 01	14200 m³/h	49.5 kW	40 kW	67 kW - HWST, 18 kW - HEX5 *	FA6-85 *	Outdoor	yes
2	Adsolair 58 19 01	14200 m³/h	49.5 kW	40 kW	67 kW - HWST, 18 kW - HEX5 *	FA6-85 *	Outdoor	yes
3	Adsolair 57 44 01	3000 m³/h	10.2 kW	8.5 kW	14 kW - HWST	/	Canadian well *	no
4	Adsolair 57 53 01	4000 m³/h	13.4 kW	10.6 kW	19 kW - HWST		Outdoor	no
5	Adsolair 58 10 01	7100 m³/h	24.6 kW	18.8 kW	20 kW - HWST	FA6-85 *	Outdoor	no
6	Adsolair 57 53 01	4000 m³/h	13.4 kW	16.6 kW	12 kW - HWST	FA6-85 *	Canadian well *	no

Table 3: Summary of HVAC equipment types, nominal properties and configuration. Unmodelled equipment components are indicated with *

ID	Description	Manufacturer	Type	Design size	Heat/cold source	Modelled
VAV	Variable air volume	Trox	TVA/TVZ 160 easy	580 m³/h	HPx	yes
CCA1	CCA north	Uponor	Contec	/	HPx or HEX1	yes
CCA2	CCA south	Uponor	Contec	/	HPx or HEX1	yes
CC	Chilled ceiling			/	HPx or HEX1	no
HP1	Heat pump	Viessmann	Vitocal 300G BW301.A29	29 kW	HEX2	yes
HP2	Heat pump	Viessmann	Vitocal 300G BW301.A29	29 kW	HEX2	yes
HP3	Heat pump	Viessmann	Vitocal 300G BW301.A45	45 kW	HEX2	yes
HP4	Heat pump	Viessmann	Vitocal 300G BW301.A45	45 kW	HEX2	yes
HEX1	Heat exchanger	Alfa laval	M10-MFM	110 kW	BF	yes
HEX2	Heat exchanger	Alfa laval	M10-MFM	240 kW	BF	yes
BF	Borefield	Moors ecoforage	25mm double U	2937 m	thermal mass	yes
HWST	Hot water storage tank		Stratified	21 m³	HEX3 and HEX4	yes
HEX3	Heat exchanger	Alfa laval	CB20	60 kW	SOL	yes
HEX4	Heat exchanger	Alfa laval	CB30	100 kW	PEL	yes
SOL	Solar collector	Viessmann	Vitosol 200T	62 m²	sun	yes
PEL	Pellet furnace	Fröling	TMC 100	100 kW	wood pellets	yes
DHW1	Domestic hot water	Viessmann	Vitocell 100C	500 l	HWST	yes
DHW2	Domestic hot water	Viessmann	Vitocell 100C	500 l	HWST	yes
DHW3	Domestic hot water	Viessmann	Vitocell 100C	500 l	HWST	yes
RAD	Radiators entrance	Zehnder		7 kW	HWST	no
IT	Cooling data center			86 kW	CWST	no
CWST	Chilled water storage tank			1000 l	CH	no
CH	Chiller	Menerga	Hybritemp 97 10 01	88 kW	outdoor air	no
HEX5	Heat exchanger	Alfa laval	CB76	86 kW	AHU1 and AHU2	no

Table 4: Summary of the CCA, borefield and solar collector controller subsystem modes. Other modes are discussed later.

	I	1	2	3	4	5
CCA collector	c	cooling	transition	off	transition	heating
Borefield	b	off	heating	cooling	heating alarm	cooling alarm
Solar	s	off	solar	solar + furnace	T_{max}	charge

strategy of the active cooling circuit is therefore omitted. This discussion is based on the interpretation of a pdf export of the block schematics of the PCD3 controllers. Parameter values and fixed offsets such as safety margins that are added to variable comparisons are generally not discussed to maintain readability of the text. Hysteresis controllers are used for all less or greater than comparisons of real variables. Whenever appropriate, we first discuss how the controller modes are computed and then how these modes determine valve and pump control signals.

Concrete core activation Hysteresis controllers compare the Running Mean Average Outdoor Temperature (RMAOT) of the last three hours and the last three days against thresholds associated with circuits CCA1, CCA2 and CC. The hysteresis controller output determines for each circuit whether cooling, heating, or neither of the two is *requested*. The majority of such requests determines whether heat or cold is requested from the collector. When the number of heating requests is the same as the number of cooling requests, heating has priority. When a switch to heat or cold demand occurs, it is maintained for a minimum duration of 1 hour. The request determines the collector mode. Its possible values are summarised in Table 4. The collector mode I_c changes value to

$$I_{c,next} = \min(5, \max(1, I_c + \Delta I_c)) \tag{1}$$

when

$$I_{c,next} \neq I_c \tag{2}$$

has been true for 240 consecutive seconds and where ΔI_c equals +1 when heat is demanded, -1 when cooling is demanded and otherwise

$$\Delta I_c = \text{if } I_c == 3 \text{ then } 0 \text{ else sign}(3 - I_c) \tag{3}$$

such that mode evolves towards $I_c = 3$.

The CCA circulation pump of a circuit is enabled when $I_c \in \{1, 2, 4, 5\}$ and heating or cooling is requested for that circuit. A cooling mode cooling curve and a heating mode heating curve based on the RMAOT for each of the CCA and the Chilled Ceiling (CC) circuits, determine the supply temperature set point for the respective circuit. The value of I_c determines which of the two heating curves is used. This temperature set point is tracked using a PI controller and a three-way valve. When no heating or cooling is requested, the valve output equals zero. To ensure that the temperature set point can be maintained, supply temperatures $T_{req,cca1}$ and $T_{req,cca2}$ are requested from the heat production controller. A similar temperature is requested for the chilled ceiling of floor 4. This temperature is omitted from the rest of the discussion since the fourth floor is not modelled in the main model.

Each individual CCA section has a two-way valve and a PI controller that control the flow rate of that section such that the return water temperature set point for that section is obtained, when possible. The return water temperature set point equals the sum of the temperature set point $T_{set,i}$ of zone i and an offset. The offset is computed using the cooling curve and heating curve, respectively in cooling and heating mode. Both curves depend on the RMAOT. The PI controller output has a lower bound larger than zero to ensure that water is always flowing, such that the return water temperature is measured correctly. Heating/cooling curve shapes and the PI controller minimum output value can be changed individually for each CCA section.

9

Variable air volume units Each VAV has a room temperature set point that equals the sum of the user-determined set point $T_{set,i}$ and an offset that is computed using a heating curve based on the RMAOT. A PI controller compares the temperature set point with the mean of the VAV return *air* temperature and a wall-mounted temperature sensor. The PI controller output is mapped linearly to $T_{set,vav,i}$, which is a supply *air* temperature set point between 16 °C and 26 °C. A second PI controller tracks $T_{set,vav,i}$ by controlling the heating coil supply water two-way valve. The resulting valve opening is upper bounded by a third PI controller that limits the heating coil return *water* temperature to 35 °C. The VAV control signal $y_{vav,i}$ equals the maximum of the outputs of a fourth and fifth PI controller, which track the CO_2 concentration set point of 1000 ppm and the room temperature set point.

Heating coil valves are enabled only when the RMAOT crosses a threshold. A heating curve based on the RMAOT then determines the supply *water* temperature set point, which is tracked using a PI controller and a three-way valve. Two more PI controllers ensure that the return *water* temperature does not exceed 40 °C or drops below 10 °C. A second heating curve determines what temperature $T_{req,vav}$ is requested from the heat production system. When all valve openings are less than 15 % then $T_{req,vav}$ is set to 15 °C. The VAV heating coil supply water pump, pump 7 in Figure 3, is enabled if a RMAOT threshold is crossed and the maximum valve opening of the VAV heating coils exceeds 5 %.

Air handling units AHU1 and AHU2 each have a supply and return duct pressure set point, a supply air temperature set point, a supply air absolute humidity set point and an on/off control signal.

Each AHU controller has a mode that determines the on/off signal of the AHU. The control logic that defines this mode could however not be interpreted due to an incomplete export of the control strategy. Therefore, the measured on/off signal of the AHUs is used in the simulations. The fixed duct pressure set points are configured using the BMS. Each of their values is 270 Pa during the verification period. The humidifiers are not modelled and therefore their control strategy is not discussed. The supply air temperature set point of an AHU equals

$$T_{set,AHU} = \text{if } \min(\mathbf{T}_{set,vav}) > T_{RMAOT} \text{ then } \min(\mathbf{T}_{set,vav}) \text{ else } \text{mean}(\mathbf{T}_{set,vav}) \tag{4}$$

where $\mathbf{T}_{set,vav}$ is the set of supply temperature set points of VAVs that are connected to the AHU and T_{RMAOT} is the running mean average outdoor temperature.

Each AHU heating coil pump is enabled when the heating coil valve is opened for more than 5 % between 6:00 and 20:00 on weekdays. The heating coil valve is controlled using a PI controller that tracks the supply temperature set point of the AHU. The PI controller is only enabled when the dampers are fully closed or fully opened and when both the chiller and adiabatic cooling are disabled.

A pump supplies water from the HWST to the AHU heating coil pumps. Similar to the VAV heating coil circuit, the supply temperature set point $T_{set,ahu}$ is computed from the RMAOT using a heating curve and the pump is enabled when a RMAOT threshold is crossed and one of the three-way valve openings y_{ahu} is at least 5 % . The supply temperature set point is tracked using a PI controller and a three-way valve. The PI controller output is upper bounded by a PI controller that ensures a maximum return water temperature of 35 °C and lower bounded by a PI controller that ensures a minimum return water temperature of 10 °C. Temperature

$$T_{req,ahu} = \text{if } y_{ahu} > 0.2 \text{ then } T_{set,ahu} \text{ else } 0 \tag{5}$$

is requested from the heating system.

$T_{req,rad}$ is a similar temperature request for the radiators. Since the radiators are not modelled, this is not discussed further.

The internal control strategy of the AHUs is presented by Jorissen et al. (2018a).

Geothermal borefield and heat pumps   The geothermal borefield mode I_b has five possible values that are summarised in Table 4. The two alarm modes are not implemented and are therefore not discussed. The geothermal borefield mode is determined using the CCA collector mode. It is in heating mode when $I_c == 5$, it is in cooling mode when $I_c == 1$ and otherwise it is off.

The heat pump control system is enabled ($s_{HP} = $ True) if $s_{HP} \equiv I_b \in \{2, 3, 4, 5\}$. The heat pumps are controlled using a cascade of 9 PI controllers that compare the heat pump supply temperature set point $T_{set,HP}$ with the supply temperature T_{sup}. The next PI controller in the sequence is enabled when the previous PI controller reaches an output of 1. The number of activated PI controllers determines the heating stage and determines which combination of heat pumps is active, i.e. whether status variables s_{HP1}, s_{HP2}, s_{HP3} and s_{HP4} are True or False. $T_{set,HP}$ is computed from the maximum of the requested supply temperatures as

$$T_{set,HP} = \text{if } I_c \in \{5\} \text{ then } \max(T_{req,vav}, T_{req,cca1}, T_{req,cca2}) \text{ else } T_{req,vav}. \tag{6}$$

T_{sup} equals the measured supply temperature of the circuit that determines $T_{set,HP}$. Moreover, the three-way valve of the circuit that determines the requested temperature is opened fully. This ensures that heat from the heat pump is not rejected, e.g. if all four collector three-way valves are closed.

When a heat pump is activated, a cascade is triggered that first opens the heat pump evaporator two-way valve. One minute later, the evaporator pump and another minute later the condenser pump and the condenser three-way valve PI controller are enabled. One more minute later the heat pump is activated. When the heat pump is deactivated, the reverse cascade is executed. The three-way valve PI controllers ensure that the condenser inlet temperatures are larger than 15 °C and output a control signal of 0 when they are off. Furthermore, the heat pump control system reduces the heating stage when the return water temperature is higher than 40 °C or when $T_{hex,HP}$, the winter heat exchanger outlet temperature at the borefield side (see Figure 3 'Echangeur Hiver'), is lower than 3 °C.

The frequency controlled borefield circulation pump is enabled if

$$I_b \in \{3, 4, 5\} \vee (s_{HP} \wedge (s_{HP1} \vee s_{HP2} \vee s_{HP3} \vee s_{HP4})) \tag{7}$$

where s_{HP1}, s_{HP2}, s_{HP3} and s_{HP4} are the on/off control signals of the four heat pumps. The pump speed equals the maximum of the pump speeds requested by the heat pumps $y_{req,HP}$, and by the CCA cooling system $y_{req,cca}$. $y_{req,HP}$ equals the minimum of two PI controller outputs that try to maintain a temperature of 15 °C for $T_{hex,HP}$ and a temperature difference of 2 K between the winter heat exchanger primary (borefield side) inlet temperature and its secondary (heat pump side) outlet temperature. $y_{req,cca}$ equals the output of a PI controller that tracks a summer heat exchanger (see Figure 3 'Echangeur Eté') supply temperature of 17 °C. This heat exchanger supplies chilled water to the CCA collector through a pump and a two-way valve that controls the amount of recirculation through a bypass (see Figure 3 pump '17' and valve 'U'). The pump is enabled if $I_b \in \{3, 4, 5\}$ and its frequency controller and the valve are controlled such that the mass flow rate through the bypass is minimised, based on temperature measurements.

Domestic Hot Water (DHW) storage tanks   Three storage tanks of 500 l with integrated heat exchangers supply domestic hot water to the building. They each have a temperature set point of 45 °C or 55 °C depending on a time schedule. A tank charging state becomes active when the measured tank temperature is lower than the set point, or when one of the other boiler charging states *becomes* active. While the state is active, the set of heat request temperatures $\mathbf{T}_{req,DHW}$ equals the temperature set points plus 10 K. Whether heat delivery is requested, is indicated by

$$\mathbf{s}_{req,DHW} = \mathbf{T}_{req,DHW} > 20°C. \tag{8}$$

If the main Hot Water Storage Tank (HWST) top temperature T_{HWST} is smaller than any element of $\mathbf{T}_{req,DHW}$ for which heat delivery is requested, then heat *production* is requested such that $s_{req,DHW,pro} = true$. Otherwise $s_{req,DHW,pro} = false$.

The DHW three-way valves are closed when the charging state is not active, or when the inlet temperature is lower than the DHW tank temperature. Otherwise the valve is fully opened if the DHW HEX return water temperature is smaller than T_{HWST}. Otherwise a common PI controller determines the three valve openings such that the temperature of the water that enters the HWST equals T_{HWST}. The three-way valve pump is enabled when the valve control signal is larger than 2 %. The DHW tanks are charged further than their set point up to a temperature of 70 °C, if excess heat from the solar collector or furnace is available, which is the case when the HWST is in mode 7, 9 or 10.

The tank temperature set points are increased using a time schedule to avoid the development of legionalla pneumophila. This is not modelled.

Hot Water Storage Tank (HWST)   The 21 m^3 HWST mode I_h can have 10 values based on

- the measured HWST temperatures,

- a request to allow heat production from the solar collectors or the pellet furnace,

- a request for heat delivery to the AHU heating coils, radiators (not modelled) or DHW tanks,

- and at what temperature this heat is requested.

We now describe when each mode is activated in order of decreasing priority.

The controller first checks whether heat production is requested by the AHU or radiators using

$$s_{req,col} = \max(T_{req,ahu}, T_{req,rad}) > 20°C \wedge \max(T_{req,ahu}, T_{req,rad}) > T_{HWST} \tag{9}$$

and for the DHW tanks using

$$s'_{req,DHW} = s_{req,DHW,pro} \wedge (1 \in \mathbf{s}_{req,DHW}). \tag{10}$$

If $s'_{req,DHW}$ and not $s_{req,col}$ then the mode is 8. If $s'_{req,DHW}$ or $s_{req,col}$ and the pellet furnace or solar collectors request hot water production then the mode is 4. If $s'_{req,DHW}$ or $s_{req,col}$, then the mode is 3. If the solar collectors request hot water production then the mode is 7. If the furnace has not completed its minimum on period then the mode is 5 or 10 depending on the previous value of the mode. If the furnace requests hot water production then the mode is 6 or 9 depending on the previous value of the mode. If $1 \in \mathbf{s}_{req,DHW}$ then the mode is 2, otherwise it is 1.

The ten modes I_h can be summarised as follows:

1. Hot water is available for the radiators and AHUs.

2. Hot water is used by the DHW tanks and is available for the radiators and AHUs.

3. Hot water is produced because of a request from the load.

4. Hot water is produced because of a request from the load and the production.

5. Hot water is produced because the furnace has not completed its minimum on period.

6. Hot water is produced because of a request from the furnace.

7. Hot water is produced because of a request from the solar collectors.

8. Hot water is produced because of a request from the DHW tanks only.

9. Hot water is produced, after a period of mode (8), because of a request from the furnace.

10. Hot water is produced, after a period of mode (8), because the furnace has not completed its minimum on period.

Based on these modes the positions of three two-way valves, denoted using α, β, γ in Figure 3, are determined. All valves are closed in mode 1 such that water can be drawn from the HWST by the AHU heating coil and radiator pumps without inducing a flow in the unused parts of the circuit. When the DHW tanks are charged, i.e. $I_h \in \{2, 8, 9, 10\}$, valve γ is opened such that the return water from the DHW tanks flows towards the HWST or to the solar collectors. Valves α and β are opened and the circulation pump is enabled when any of the production devices is enabled, i.e. $I_h \notin \{1, 2\}$. A PI controller tracks the hot water supply temperature set point $T_{set,sup}$ using the pressure-independent valve that is connected in series with pump 11. $T_{set,sup}$ is determined using I_h, $\max(\mathbf{T}_{req,DHW})$ and $T_{req,hwst}$, the temperature that the AHU controller and the radiator controller request to be available in the tank.

The described control strategy causes valves β and γ to be opened simultaneously when $I_h \in \{8, 9, 10\}$. The hot water flow can then pass through the two opened valves or through the hot water storage tank, and their relative flow rate depends on the flow friction of the two paths, which is unknown. From a discussion with the engineering firm that designed the HVAC system, the reason for allowing two flow paths could not be identified. In the model we therefore altered the control strategy such that there is only one possible flow path in each mode. I.e. in mode 9 only valve β is opened since the relatively low discharge thermal power and the therefore also relatively low circuit flow rate would cause a large flow rate to be drawn from the HWST top by the DHW tank pumps. During modes 8 and 10 the furnace is at full power and charging the DHW tanks. The DHW tank outlet temperature is then connected to the furnace inlet pipe by opening valve γ.

Solar collector The solar collector mode I_s is determined using I_h, the solar heat exchanger secondary outlet temperature $T_{hex,sol}$, the HWST top and bottom temperatures and the solar collector temperature.

When the solar collector temperature exceeds 55 °C, a flip-flop is set to true, which enables mode 5, which is the charging mode. When $T_{hex,sol}$ exceeds $T_{req,hwst}$ the solar controller requests that it may produce hot water, which affects I_h. If $I_h \in \{7\}$, then mode 2 is activated. If $I_h \in \{4, 5, 8\}$ and the flip-flop output equals true and $T_{hex,sol}$ is larger than $T_{sol,in}$, the inlet temperature of the solar circuit, then the solar collector is in mode 3 or 4. In these modes the solar collector and furnace are enabled simultaneously. If the supply temperature is sufficiently high such that $T_{hex,sol} > T_{req,hwst}$ then the mode is 4. The flip-flop is reset when $T_{hex,sol}$ drops below $\min(T_{sol,th}, T_{sol,in})$.

Both solar collector pumps are activated when $I_s \in \{2, 3, 4, 5\}$. The three-way valve is only opened when $I_s \in \{2, 3, 4\}$. Its valve opening is computed using two PI controllers. The first PI controller tries to control the flow rate such that it equals the flow rate of the HWST pump, based on temperature measurements. This output is upper bounded by the second PI controller that maintains a temperature difference of at least 5 K between $T_{hex,sol}$ and $T_{sol,in}$.

Pellet furnace The pellet furnace mode I_f can have 9 values that are summarised here in order of decreasing priority. Mode 2 is activated if $I_h \in \{3\}$, which starts heat production. Modes 3 or 7 are activated if $I_h \in \{4, 8\}$, when heat is being produced. If the furnace has not yet completed its minimum on period or if $I_h \in \{5, 10\}$ then the mode is 4 or 8. Otherwise the mode is 5 or 9 if $I_h \in \{6, 9\}$ or if the furnace heat exchanger secondary supply temperature exceeds 70 °C. In these latter modes, residual heat from the furnace is discharged into the circuit. If none of the above modes are selected then the furnace is off and the mode is 1. Mode 6 is unused. Whether mode 3 or 7, 4 or 8 and 5 or 9 are active, depends on the same condition; the former mode is active unless i) the furnace three-way valve opening exceeds 70% or $I_h \in \{4, 8\}$, and ii) the heat exchanger secondary supply water temperature $T_{hex,pel}$ exceeds the requested tank temperature $T_{req,hwst}$. Modes 7, 8 and 9 are the 'Tmax' modes, which indicate that a temperature $T_{req,hwst}$ can be produced by the furnace. The PI controller that

controls the pressure-independent valve of pump 11 is only activated when this condition is satisfied, or when the solar collector is able to supply the requested temperature, i.e. $I_s \in \{2, 4\}$.

The modes can be interpreted as follows:

1. The furnace is off.

2. The furnace is enabled, hot water production is starting.

3. The furnace is enabled and hot water is being produced.

4. Hot water production is not required, but the furnace has not completed its minimum on period.

5. The furnace is off and residual heat is being discharged.

6. Mode 2 + Tmax: the pump of the main circuit is enabled

7. Mode 3 + Tmax: the pump of the main circuit is enabled

8. Mode 4 + Tmax: the pump of the main circuit is enabled

9. Mode 5 + Tmax: the pump of the main circuit is enabled

The furnace is enabled when $I_f \in \{2, 3, 7\}$. It then stays on for at least 2 hours. During this period a flag is sent to the HWST controller indicating that the minimum on time has not completed. The furnace pump is activated while the measured furnace temperature exceeds 70 °C or when the furnace's integrated controller requests the pump to be on. The heat exchanger pump is activated when $I_f \in \{3, 4, 5, 7, 8, 9\}$. The three-way valve control signal is determined using three PI controllers. The first PI controller tries to control the flow rate such that it equals the flow rate of the HWST pump, based on temperature measurements. Its output value is upper bounded by two other PI controllers that ensure a furnace inlet temperature of at least 62 °C and a temperature difference of at least 5 K between the water that enters and leaves the furnace subcircuit. While the furnace pump is on, a request is sent to the HWST controller to allow the furnace to supply heat to the system.

Valve models Solarwind mostly uses two-way and three-way valves with linear and equal-percentage opening characteristics. One pressure-independent valve is used in series with pump 11 in Figure 3. It is not drawn on the HVAC plan, but does exist in practice. Linear two-way valves are modelled using `IBPSA.Fluid.Actuators.Valves.TwoWayLinear`. `IBPSA.Fluid.Actuators.Valves.TwoWayEqualPercentage` was not used to model the equal-percentage valves, since the used valves do not have a pure equal-percentage opening characteristic. Instead, they have a linear opening characteristic between 0% and 30% and a equal-percentage characteristic after that. This has been modelled by creating a new valve model `IBPSA.Fluid.Actuators.Valves.TwoWayPolynomial` which accepts a set of polynomial coefficients as model parameters. The used polynomial is

$$y'(t) = 0.5304y(t) - 0.7698y(t)^2 + 1.2278y(t)^3 \tag{11}$$

where $y(t)$ is the valve control signal and $y'(t)$ is the polynomial result. This value is used to compute the valve k value as

$$k(t) = K_v \left[l + y'(t)(1 - l) \right] \tag{12}$$

where l is the valve leakage and K_v is a valve parameter (Wetter et al. 2015).

Our three-way equal-percentage valves use the same polynomial implementation.

To actuate the valves, Siemens SQS 65 motors are used. These actuators have a linear or equal-percentage (default) valve opening characteristic for a control signal between 0 V or 2 V and 10 V. The values of these two actuator settings are unknown and were therefore fitted from measurement data where possible.

2.4 Building Measurements

The BMS uses many sensors that can be deployed for verification and debugging purposes. The installed sensors are summarised here.

Each VAV has a supply air temperature sensor, a return air temperature, relative humidity and CO_2 sensor. Zones have one or more wall-mounted temperature sensors. The VAV heating coil return water temperature is measured. Moreover, the return water temperature and concrete core temperature of most CCA slabs are measured. A Davis instrument Vantage pro 2 weather station on the roof monitors the outdoor temperature and humidity, barometric pressure, wind speed and direction and solar irradation on a vertical west, south and east oriented surface. The AHU supply and return air volumetric flow rates, temperatures and humidities, and the duct pressures are measured. Furthermore, various types of temperature sensors and thermal energy meters (heat meters) are installed throughout the hydronic system and the electrical power use for lighting and appliances is measured separately per zone. Additional electrical power meters are installed for large loads such as the heat pumps and AHUs. The sensor types and accuracies are summarised in Table 5. For more information we refer the reader to the respective data sheets.

Many, but not all of these sensors are logged. In addition to the sensor readings, some of the BMS control signals and internal variables such as the RMOAT, are logged. Throughout this text sensor measurements and these BMS variables are both referred to as *measurements*. Due to hardware constraints, the maximum number of measurements that can be stored simultaneously is limited. At the time of writing about 1300 measurements are logged. By default, each measurement is stored together with a MySQL timestamp when a preconfigured threshold value relative to the previously stored value is exceeded.

The measurements were exported as a MySQL database dump, which is post-processed using Matlab. When multiple measurements are stored within the same second, the oldest samples, i.e. those with the lowest MySQL primary key values, are discarded. Continuous measurements are interpolated using zero-order hold interpolation. The interpolated signal is resampled to 2-minutes averaged data by computing the average of 15 equidistant samples of the interpolated data within each 2-minutes interval. The resulting data is used in the simulations, where the data is linearly interpolated. Discrete measurements such as boolean or integer BMS variables are not resampled.

Since not all variables can be logged, a selection had to be made. Therefore, some partly redundant sensors are not logged. For instance, some zones have three VAVs that each extract return air at the same point in the zone. Therefore the return air temperature is the same for the three extractions and since the temperature set point is also the same, the VAV control signal and heater valve openings are often as well the same since they operate using very similar inputs. Therefore only one of the three VAV measurements is logged. In the verifications we assume that all three control signals have the same value.

3 Model Implementation

We now discuss in more detail how various components are modelled in Modelica for respectively the building envelope, HVAC system and control. References to published material are made where possible.

3.1 Building Envelope

Most used building models originate in the IDEAS library, which is described by Jorissen et al. (2018b). In addition to this a custom zone air model was developed to simulate the under-floor air distribution system, and a discretised floor was used to model the concrete core activation more accurately. These models are discussed here. Furthermore, a model for computing the diffuse and beam solar irradiation from measurements of the solar irradiation on three vertical surfaces, and shading models are presented. Afterwards important building parameters of existing IDEAS models are discussed.

Table 5: Summary of the installed sensors.

Manufacturer	Type	Description	Accuracy	Location, comments
Sosomec	Countis E33	Electrical power	IEC 62053-21 - class 1	AHU, Electrical power of lighting and appliances
Sosomec	Diris A20	Electrical power	0.5 % [W]	Heat pump, circulation pumps
Kamstrup	Multical 402	Heat meter	1.15 % [W]	Heating coil AHU, CCA, Solar, Furnace, Boilers
Kamstrup	Multical 601	Heat meter	1.15 % [W]	Heat pump, borefield
S+S Regeltech.	Thermasgard ETF	Immersion temp.	$\pm$ 0.4 K	Hydronics
Siemens	QAA20 series	Wall-mounted T	$\pm$ 0.4 K	Wall-mounted zone temperature
Siemens	QAE21 series	Immersion temp.	$\pm$ 0.7 K	Hydronics
Siemens	QFM21 series	Air T, RH	5 % RH, 0.8 K	Air sensor
Siemens	QPM21 series	Air CO_2	50 ppm $\pm$ 2 %	Air sensor, drift of $\approx$ 20 ppm/year
Davis	Vantage pro	Weather station	3 % RH, 5% W/m^2, 0.5 K, max(3 km/h, 5%), 3 ° [wind direction]	

3.1.1 Under-floor Air Distribution Model

The default IDEAS air model assumes that air is perfectly mixed, which is not the case here since an under-floor air distribution system is used. Therefore a more detailed model was needed.

Lin and Linden (2005) present a UFAD model based on plume theory and laboratory experiments. Their results form the basis for the EnergyPlus *under-floor air distribution interior zone* model. The EnergyPlus model computes the return air temperature as (U.S. Department of Energy 2017, Equation 13.180)

$$T_{ret} = T_{sup} + \frac{0.0281\dot{Q}}{1000\dot{V}g}T_{sup}, \tag{13}$$

where T_{sup} [K] is the supply temperature, $\dot{Q}$ [W] is the net heat flow rate that is injected in the zone air, $\dot{V}$ [m^3/s] is the volumetric flow rate, $g \sim \frac{\dot{V}^{3/2}}{\dot{Q}^{1/2}}$ is a dimensionless parameter with typical values in the range of 2 - 15 (U.S. Department of Energy 2017, Figure 13.16). However, using conservation of energy we expect that

$$T_{ret} = T_{sup} + \frac{\dot{Q}}{c_p\rho\dot{V}}. \tag{14}$$

Based on our understanding of the model equations, these two equations are incompatible and implementing (13) would thus lead to a violation of conservation of energy, which we do not consider to be acceptable.

Since no further UFAD models were found, we now discuss related research for modelling Displacement Ventilation (DV). DV does not have multiple vents in the floor, but rather uses a single supply vent that is typically located in a wall instead of in a floor. UFAD in general leads to less stratification since the air flow has more upward momentum, which induces mixing. Webster et al. (2002) however showed a large degree of stratification for low flow rates. Solarwind has a nominal flow rate that corresponds to the lower range of the presented study. Therefore we assume that the UFAD system has a degree of stratification similar to DV, such that DV models are also applicable.

Li et al. (1992) and Hensen and Hamelinck (1995) propose nodal models for DV. Rees and Haves (2001) however argue that these 'one-dimensional plug flow' models over-estimate the wall and room air temperatures. They therefore propose a model that subdivides the room into four stacked nodes of equal height and a second set of air nodes that represent thermal plumes. This model uses separate convection coefficients for the four air layers and computes the wall heat exchange for each of the four segments using a different wall temperature. IDEAS only considers a single wall temperature. Rees and Haves' model uses ten nodes in total. The flow rate of the mass entrained into these plumes is a model parameter that needs to be determined for each of the air layers. Average parameter values were provided by Rees and Haves (2001) but it is unclear whether they are applicable.

Wu et al. (2013) present a nodal model that has three vertically stacked nodes and a fourth node for the downdraft generated by external walls and windows. The downdraft flow rate computation however does not support a negative temperature difference ΔT_{dd}, which may occur during summer, since $\Delta T_{dd}^{0.4}$ is computed, which is undefined for negative values of ΔT_{dd}. Moreover, this model does not treat thermal plumes separately. Due to the relatively large internal gains of the model and the well insulated walls, the thermal plume model is assumed to be more important. Mateus and Carrilho da Graça (2015) propose a three-nodes model that computes the height of the mixed upper air layer (neutral height) using a thermal plume model. This variable height is however incompatible with IDEAS, which considers a single wall temperature. Moreover, the equations result in a *neutral height* of 0 m whenever the ventilation is disabled, which raises the question whether the equations are still valid when the ventilation system is disabled. For these reasons a custom model was developed similar to the model of Wu et al. (2013), without the downdraft model and with a thermal plume model.

The zone air model divides the zone air into three nodes that are stacked vertically and have temperatures $T_{top}(t)$, $T_{mid}(t)$ and $T_{bot}(t)$. Their associated air volumes are $V_{top} = 0.2V$, $V_{mid} = 0.7V$

and $V_{bot} = 0.1V$ where V is the total zone air volume.

Convective heat transfer with a heat flow rate $\dot{Q}_{con}$ occurs between the top, bottom and middle nodes and respectively the ceiling, floor and walls and windows. For the ceiling, walls and windows, the default IDEAS natural convective heat transfer correlations from Awbi and Hatton (1999) are used. However, forced convection occurs at the floor when the displacement ventilation is activated and otherwise natural convection occurs. These two effects are combined using the correlations from (Novoselac et al. 2006, Table 4) such that the floor convective heat transfer coefficient $h_{flo}(t)$ equals

$$
h_{flo}(t) = \begin{cases} \left[\left(\frac{2.175\Delta T(t)^{0.308}}{D_h^{0.076}} \right)^6 + \left(0.48 \frac{|T_{flo}(t) - T_{sup}(t)|\mathrm{ACH}(t)^{0.8}}{\Delta T(t)} \right)^6 \right]^{1/6}, & \text{if } T_{flo}(t) \geq T_{top}(t) \\ \left[\left(\frac{0.704\Delta T(t)^{0.133}}{D_h^{0.601}} \right)^6 + \left(0.48 \frac{|T_{flo}(t) - T_{sup}(t)|\mathrm{ACH}(t)^{0.8}}{\Delta T(t)} \right)^6 \right]^{1/6}, & \text{otherwise} \end{cases} \tag{15}
$$

where $\Delta T(t) = T_{flo}(t) - T_{bot}(t)$, $T_{flo}(t)$ is the floor temperature, D_h is the hydraulic diameter of the floor, $\mathrm{ACH}(t)$ is the air change rate per hour and $T_{sup}(t)$ is the supply air temperature. The convective heat flow rate towards the bottom node then equals

$$
\dot{Q}_{con} = A_{flo} h_{flo}(t) \Delta T(t) \tag{16}
$$

where A_{flo} is the surface area of the floor.

Advection causes heat and mass transfer between the three nodes. Supply air with flow rate $\dot{m}_{sup}$ is injected in the bottom node and return air with a flow rate $\dot{m}_{ret}$ is extracted from the top node. Flow rate imbalances between the supply air and the return air are compensated by a flow rate injection or extraction from the middle node.

The nodes also exchange heat when unstable stratification occurs. In these cases we assume that the zone air becomes well-mixed, by exchanging heat between the nodes using a time constant τ of 180 s such that

$$
\dot{Q}_{mid \to top}(t) = \frac{V\rho c_p}{\tau} \max(T_{mid}(t) - T_{top}(t), 0)^{1.33} \tag{17}
$$

$$
\dot{Q}_{bot \to mid}(t) = \frac{V\rho c_p}{\tau} \max(T_{bot}(t) - T_{mid}(t), 0)^{1.33} \tag{18}
$$

where ρ is the density of air, c_p is the specific heat capacity of air. The exponent 1.33 is added since this exponent is used to model natural convection between a heated floor and air. Note that the real model time constants are smaller than τ since $V_{bot} = 0.1V$.

Convective internal heat gains $\dot{Q}_{con,int}(t)$ from appliances and occupants are injected into the top node using a simplified thermal plume model. This model assumes that the mass flow rate $\dot{m}_{plm}(t)$:

$$
\dot{m}_{plm}(t) = \frac{\dot{Q}_{con,int}(t)}{7.5 c_p} \tag{19}
$$

from the middle node is entrained with the heat such that the resulting thermal plume has a temperature of 7.5 K above the middle node temperature. This temperature difference was estimated based on results from Rees and Haves (2001).

Taking into account that some specific flow rates can cancel each other, the resulting differential

equations for the energy balance are then

$$0.2\rho V c_p c_m \frac{\mathrm{d}T_{top}(t)}{\mathrm{d}t} = \dot{Q}_{con,int}(t) + \dot{Q}_{mid\to top}(t) + \sum_i \dot{Q}_{ceil,i}(t) +$$

$$c_p \max\left[\dot{m}_{ret}(t), \dot{m}_{plm}(t)\right]\left[T_{mid}(t) - T_{top}(t)\right],$$

$$0.7\rho V c_p c_m \frac{\mathrm{d}T_{mid}(t)}{\mathrm{d}t} = -\dot{Q}_{mid\to top}(t) + \dot{Q}_{bot\to mid}(t) + \sum_i \dot{Q}_{wall,i}(t)$$

$$+ c_p \dot{m}_{sup} T_{bot}(t) + c_p \dot{m}_{plm} T_{top}(t)$$

$$+ c_p \max\left[0, \dot{m}_{plm}(t) - \dot{m}_{ret}(t)\right] T_{top}(t) - c_p \max\left[\dot{m}_{ret}(t), \dot{m}_{plm}(t)\right] T_{mid}(t)$$

$$+ c_p \max\left[0, \dot{m}_{ret}(t) - \dot{m}_{sup}(t)\right] T_{air,ext}(t) + c_p \min\left[0, \dot{m}_{ret}(t) - \dot{m}_{sup}(t)\right] T_{mid}(t)$$

$$+ c_p \dot{m}_{inf}(t)\left[T_{air,ext}(t) - T_{mid}(t)\right],$$

$$0.1\rho V c_p c_m \frac{\mathrm{d}T_{bot}(t)}{\mathrm{d}t} = -\dot{Q}_{bot\to mid}(t) + \sum_i \dot{Q}_{flo,i}(t) + c_p \dot{m}_{sup}(t)\left[T_{sup}(t) - T_{bot}(t)\right],$$

where $T_{air,ext}$ is the exterior dry bulb temperature, $\dot{m}_{air,inf}$ is the air infiltration flow rate, and $c_m = 5$ is a factor that artificially enlarges the air thermal mass (Sourbron 2012, Table D.4). The infiltration flow rate $\dot{m}_{air,inf}$ is computed assuming an n50 value of 0.25 ACH, which was measured using a blower door test on the full building. A constant air leakage rate corresponding to 0.25/20/h is assumed for each zone. The division by 20 is a best estimate of the real infiltration based on the n50 value. This estimate simplifies aspects such as wind shielding, stack effect and the type of leaks (Meier 1994). As explained by Meier (1994), this value is likely an underestimation for Solarwind since the stack effect is stronger for tall buildings. These three differential equations are slightly simplified since IDEAS uses humidity-dependent enthalpies instead of temperatures for the actual computations.

3.1.2 Discretised CCA floor model

The embedded pipe model by Koschenz and Lehmann (2000) is used to model heat transfer between the concrete core activation slab and the embedded pipe in the concrete. This model has a lower bound for the mass flow rate, for which the model is valid. This lower bound can be reduced by discretising the model along the water flow direction. The embedded pipe model, and therefore also the floor, were discretised into three sections such that low flow rates are modelled sufficiently accurately. Moreover, part of the concrete floor slab does not contain embedded pipes and is thus not activated. The floors were therefore discretised in four parts. The first three parts are connected to the embedded pipes and each contains one third of the total activated floor area. The total activated floor was determined using plans containing the dimensions of the CCA sections, as illustrated by Figure 4. The remaining floor surface area was attributed to the fourth part.

3.1.3 Computation of beam and diffuse solar irradiation

The building weather station measures the total solar irradiation on three vertical surfaces that are parallel to the east, south and west sides of the building, see Figure 5. IDEAS however uses $H_{dir}(t)$ and $H_{dif}(t)$ as inputs, which are the direct beam solar irradiation and the diffuse solar irradiation on a horizontal surface. A model is developed for deriving the IDEAS inputs from the measurements. This model is described here.

The Perez model (Perez et al. 1987),(Perez et al. 1990) could be used to compute the total solar irradiation on the three inclined surfaces as

$$H_{eas}(t) = \mathrm{Perez}(H_{dir}(t), H_{dif}(t), \rho_{eas}, \phi_{eas}, \theta_{ver}, \mathrm{lat}, \mathrm{lon}, t) \tag{20}$$

$$H_{sou}(t) = \mathrm{Perez}(H_{dir}(t), H_{dif}(t), \rho_{sou}, \phi_{sou}, \theta_{ver}, \mathrm{lat}, \mathrm{lon}, t) \tag{21}$$

$$H_{wes}(t) = \mathrm{Perez}(H_{dir}(t), H_{dif}(t), \rho_{wes}, \phi_{wes}, \theta_{ver}, \mathrm{lat}, \mathrm{lon}, t) \tag{22}$$
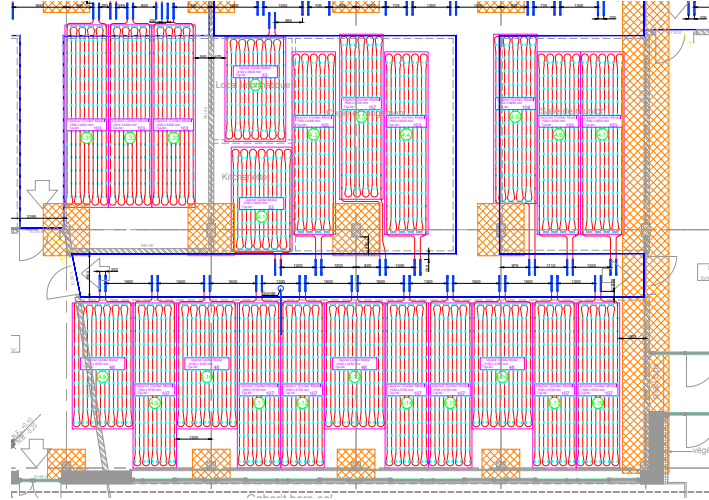
Figure 4: Illustration of CCA section dimensions that were used for determining the activated floor area.

Figure 5: Picture of the weather station solar irradiation sensors.

where ρ is the ground reflectivity, ϕ is the azimuth angle, θ_{ver} is the tilt angle (vertical), lat and lon are the building latitude and longitude and t is time, which is used to compute the solar position.

Equations (20)-(22) could be inverted to compute the unknown values of $H_{dir}(t)$ and $H_{dif}(t)$ from the known values of $H_{eas}(t)$, $H_{sou}(t)$ and $H_{wes}(t)$. This however implies that three equations would be used to compute two values, which leads to an overspecified problem. Using only two of the three equations would imply discarding some of the measured information and is expected to lead to poor results due to measurement noise.

Therefore a different approach is presented that uses all three sensors. First, the direct solar irradiation is estimated using each of the three sensors, by subtracting an estimation of the diffuse solar irradiation and the ground reflection from the measured solar irradiation on the inclined surfaces:

$$\hat{H}_{dir,i}(t) = \frac{\hat{H}_i(t) - 0.5\hat{H}_{dif}(t) - 0.5\hat{H}_{gro,i}(t)}{\cos(\theta_i)} \qquad \forall i \in \{eas, sou, wes\} \tag{23}$$

$$\hat{H}_{dif,i}(t) = \frac{\hat{H}_i(t) - 0.5\hat{H}_{gro,i}(t)}{\cos(\theta_i)} \qquad \forall i \in \{eas, sou, wes\} \tag{24}$$

$$\hat{H}_{gro,i}(t) = \rho_i \cos(\theta_i)\hat{H}_{dir,i} + \hat{H}_{dif}(t) \qquad \forall i \in \{eas, sou, wes\} \tag{25}$$

where $\hat{H}_{gro,i}(t)$ is the solar irradiation reflected by the ground in front of direction i. Factors 0.5 are used since the view factor of a vertical surface to the ground and the air is 0.5. We here implicitly assume that the diffuse solar irradiation is equally strong in all directions.

Equation (24) assumes that there is at least one direction on which no direct solar irradiation is present, such that $\hat{H}_{dif}(t)$ can be computed as

$$\hat{H}_{dif}(t) = 2 \min\left[\hat{H}_{dif,eas}(t), \hat{H}_{dif,sou}(t), \hat{H}_{dif,wes}(t)\right]. \tag{26}$$

A factor two is used since $\hat{H}_{dif,i}(t)$ is the diffuse solar irradiation measured by the sensor, which is only half of the diffuse solar irradiation that would fall onto a horizontal surface due to the view factor of 0.5. The direct solar irradiation is chosen equal to either $\hat{H}_{dir,eas}(t)$, $\hat{H}_{dir,sou}(t)$, $\hat{H}_{dir,wes}(t)$, or an interpolation between these values, depending on what corresponding surface normal has the smallest angle with respect to the sun rays. These equations form an implicit system of equations that is automatically solved by the Dymola algebraic loop solver.

Equation (24) is inconsistent with the Perez model, since the Perez model does not assume uniform diffuse solar irradiation. Instead, Perez computes the sky diffuse solar irradiation for a vertical surface as

$$H_{dif,perez}(t) = H_{dif}(t)\left[0.5(1 - F_1(t)) + F_1(t)a(t)/c(t) + F_2(t)\right] \tag{27}$$

where $F_1(t)$ and $F_2(t)$ are functions of $H_{dir}(t)$ and $H_{dif}(t)$ and $a(t)$ and $c(t)$ each are functions of the sun position and surface orientation.

Equations (24) could be replaced by (27) to obtain a more accurate approximation of the Perez model inverse, but since $F_1(t)$ and $F_2(t)$ depend on $H_{dir}(t)$ and $H_{dif}(t)$, this leads to a more complicated algebraic loop, for which no solution is found. Therefore $F_1(t)$ and $F_2(t)$ are computed using $\hat{H}_{dif}(t)$ and $\hat{H}_{dir}(t)$. The previously described equations are implemented a second time, now using (27) instead of (24) and

$$\mathbf{H}_{dif}(t) = \left\{ \frac{\hat{H}_{dif,i}(t)}{(0.5(1 - F_1(t)) + F_1(t)a_i(t)/c_i(t) + F_2(t))} : \forall i \in \{eas, sou, wes\} \right\} \tag{28}$$

$$H_{dif}(t) = \min\left(\mathbf{H}_{dif}(t)\right). \tag{29}$$

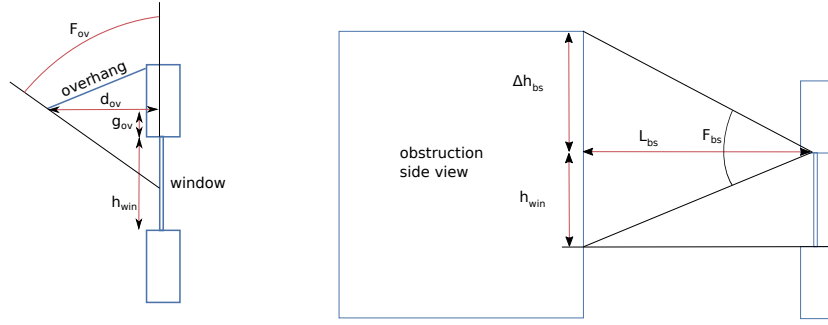instead of (26). From these equations the final values of $H_{dif}(t)$ and $H_{dir}(t)$ are computed.

Figure 6: Illustration of building and overhang diffuse shading models.

Parameter values for ρ_{eas}, ρ_{sou} and ρ_{wes} need to be determined. The value of ρ_{wes} is approximately known and chosen equal to 0.16, which is the solar reflection coefficient of the atrium glazing that is located at the south-west of the weather station. The other ground reflectivities are fitted such that the transition between the values of $\hat{H}_{dir,eas}(t)$, $\hat{H}_{dir,sou}(t)$ and $\hat{H}_{dir,wes}(t)$ is smooth. This leads to an estimated value for the east and south ground reflectivities of 0.2 and 0.1. The default ground reflectivity of IDEAS is 0.2.

Since the ground material around the building is not the same as on the roof, a different ground reflectivity is used for all walls and windows. IDEAS models do not accurately compute the ground view factor for walls and windows that are far above ground level or that are surrounded by buildings and other objects. This could lead to an overestimation of the solar gains from ground reflection. The ground reflectivity is therefore set to zero instead of the default value of 0.2.

3.1.4 Shading models

Solarwind is shaded from the outside by a combination of surrounding buildings, its own building envelope, PV panel overhangs on the south façade and controllable screens on the east and west façades. Floor -1 is also shaded by the surrounding ground.

PV panel overhangs are modelled using the IDEAS overhang model, which was described by Baetens (2015). This model is extended to include the effect of the overhang on diffuse solar irradiation. The Perez model computes the diffuse sky solar irradiation $H_{sky,i}(t)$, and the diffuse ground irradiation $H_{gro,i}(t)$ of window i. We take into account that the overhang partly blocks the sky view by computing the shaded sky solar irradiation as

$$H'_{sky,i}(t) = f_{ov,sky} H_{sky,i}(t) \tag{30}$$

$$f_{ov,sky} = 1 - \frac{\arctan\left(\frac{d_{ov}}{g + 0.5 h_{win}}\right)}{\pi} \tag{31}$$

where d_{ov} is the overhang depth, h_{win} is the window height, g_{ov} is the vertical gap between the overhang and the window top, as illustrated in Figure 6. Coefficient

$$F_{ov} = 2 \frac{\arctan\left(\frac{d_{ov}}{g_{ov} + 0.5 h_{win}}\right)}{\pi} \tag{32}$$

is an approximation of the view factor of the overhang. This model implicitly assumes that the overhang reflects no solar irradiation towards the window, it neglects edge effects, and it assumes that the diffuse solar irradiation is uniform in all directions. Overhang dimensions are obtained from building plans.
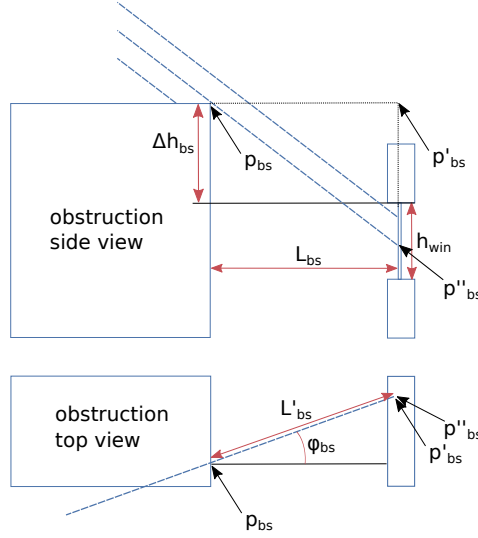
22

Figure 7: Illustration of building direct shading model using a side view and a top view.

Adjacent building wings are modelled by the IDEAS side fin model of Baetens et al. (2015), which uses a similar equation as the overhang model. We assume that the side fins block the view of the sky and the ground such that the shaded diffuse solar irradiation components are

$$H'_{sky,i}(t) = f_{sf}H_{sky,i}(t) \tag{33}$$

$$H'_{gro,i}(t) = f_{sf}H_{gro,i}(t) \tag{34}$$

$$f_{sf} = 1 - 2\frac{\arctan\left(\frac{d_{sf}}{g_{sf}+0.5h_{win}}\right)}{\pi} \tag{35}$$

where d_{sf} is the side fin depth and g_{sf} is the gap between the side fins and the window edge. The model thus assumes that no light is reflected by the side fins.

Controllable screens are modelled using the IDEAS screen model, which assumes that the transmitted direct solar irradiation varies linearly with the screen control signal. The same assumption are made for the diffuse solar irradiation components such that the shortwave solar irradiation is completely blocked when the screen is fully closed.

Surrounding buildings and ground shade, including shade from elevated surrounding ground levels for floor -1, are modelled using the IDEAS building shade model. This model assumes that light is blocked by a parallel, infinitely wide object at distance L_{bs} and with fixed height of the building top relative to the window top Δh_{bs}. These parameters are illustrated in Figure 7. The shaded direct solar irradiation $H'_{dir,i}(t)$ of window i is computed as

$$H'_{dir,i}(t) = f_{bs,dir}(t)H_{dir,i}(t) \tag{36}$$

where $f_{bs,dir}(t)$ is a shading factor that is derived as follows.

Point p_{bs} on the building edge is horizontally projected onto the window plane along the vertical plane through a sun ray. The point is thus projected onto p'_{bs} over a distance

$$L'(t) = \frac{L}{\cos(\phi_{bs}(t))} \tag{37}$$

23

Table 6: Façade layers and thermal properties ordered from outside to inside. Bold faced numbers indicate that the data originates from datasheets or plans. Other values are IDEAS default values, based on other sources or are reasonable estimates.

Material	description	d [cm]	k [W(mK)$^{-1}$]	ρ [kgm^{-3}]	c$_p$ [J(kgK)$^{-1}$]	ϵ_{lw}	ϵ_{sw}
Gypsum	Roughcast	1.25	0.25	975	840	0.85	0.65
Steico Protect	fiberboard	**4**	**0.048**	**0.23**	**2100**		
Steico Zell	wood fibre	**40**	**0.04**	**0.04**	**2100**		
OSB3	wood fibre	**1.5**	**0.13**	**640**	**4000**		
Knauf Cleaneo	interior finish	1.25	0.25	975	840	0.85	0.65

where $\phi_{bs}(t)$ is the solar azimuth angle relative to the window surface normal. p''_{bs} is the projection of p_{bs} along the sun direction, onto the window plane. Points p_{bs}, p'_{bs} and p''_{bs} form a rectangular triangle since one side is horizontal and one side is vertical. The distance between p'_{bs} and p''_{bs} can thus be computed as

$$L''(t) = L' \tan(\text{alt}(t)) \tag{38}$$

where alt(t) is the solar altitude angle: the angle between the sun rays and the horizontal plane.

If point p''_{bs} is below the window bottom such that $L''(t) > \Delta h_{bs} + h_{win}$, then the beam solar irradiation is unaffected and $f_{bs,dir}(t) = 1$. If the point is above the window top such that $L''(t) < \Delta h_{bs}$, then $f_{bs,dir}(t) = 0$. Otherwise only a fraction of the incoming beam solar irradiation is transmitted and $f_{bs,dir}(t)$ is computed as

$$f_{bs,dir}(t) = (L''(t) - \Delta h_{bs})/h_{win}. \tag{39}$$

Furthermore, the shaded diffuse solar irradiation components are computed as

$$H'_{gro,i}(t) = f_{bs,gro}H_{gro,i}(t) \tag{40}$$

$$H'_{sky,i}(t) = f_{bs,sky}H_{sky,i}(t) \tag{41}$$

Since the window height above ground level is not a model parameter, we assume that $f_{bs,gro} = 1$ and that $f_{bs,sky}$ can be approximated as

$$f_{bs,sky} = 1 - \frac{\arctan(h_{win}/L_{bs}) + \arctan(\Delta h_{bs}/L_{bs})}{0.5\pi}, \tag{42}$$

which uses a view factor that is computed as illustrated in the right of Figure 6.

3.1.5 IDEAS building envelope parameters

Floors 0 – 3 are each subdivided into eight zones, as indicated using different colors on the ground plan of floor 0 in Figure 2. Zone surface areas and wall lengths were determined from these plans. Since each floor has a height of 3.2 m, the wall height is 3.2 m. Due to the raised floor height of 30 cm and the concrete slab thickness of 25 cm, the zone height is 2.65 m.

The main façade consists of a wooden structure that is inflated with wood fibre. The façade is plastered with roughcast. The interior finish consists of perforated acoustic plasterboard and an air cavity. Since IDEAS has no models for ventilated cavities, the wall model is structured approximately as summarised in Table 6 where d is the layer thickness, k is the thermal conductivity, ρ is the density, c_p is the specific heat capacity and ϵ_{lw} and ϵ_{sw} are the longwave and shortwave emissivities.

A raised floor is used on floors 0 – 3. Its structure is summarised in Table 7. The concrete thermal conductivity of 1.8 W(mK)$^{-1}$ is based on design calculations. The data sheets indicate that the floor tiles have an aluminum bottom finish. This has been taken into account by adjusting the longwave emissivity of the tile accordingly. Heat from the embedded pipes is injected from the center, thus between the two halves of the 25 cm concrete slabs.

Table 7: Structure of the raised floors on floors 0 − 3.

Material	description	d [cm]	k [W(mK)$^{-1}$]	ρ [kgm^{-3}]	c$_p$ [J(kgK)$^{-1}$]	ϵ_{lw}	ϵ_{sw}
Intec PS34	Composite tile	**3.4**	0.6	**1500**	840	0.85	0.65
Aluminum	Tile bottom	0				0.04	0.65
Air	air	**26.6**	Convective (by Hollands et al. (1975)) and radiative heat transfer				
Concrete	concrete	**12.5**	1.8	2100	840	0.88	0.55
Concrete	concrete	**12.5**	1.8	2100	840	0.88	0.55

Table 8: Glazing properties and orientations of the used glazing types where E, S, W, N are the cardinal directions, τ_e, ρ_e and a_e are the solar energy transmission, reflection and absorption coefficients, g is the g-value and U_g is the thermal conductance of the glazing system.

Name	sheets	laminated	location	τ_e [%]	ρ_e [%]	a_e [%]	g [%]	U_g [Wm^{-2}K^{-1}]
GT 401	3	no	E+S+W	41.8	32.4	25.8	49	0.5
GT 402	3	yes	E+S+W	38.2	31.8	30.0	49	0.6
GT 404	3	no	N	26.2	38.4	35.4	31	0.5
GT 405	3	yes	N	24.8	38.4	36.8	31	0.6
GT 509	2	NA	N	41.0	22.0	37.0	55	1.0
60/28	3	yes	N	21.2	40.9	37.9	25	0.6

The roof of floor 3 consists of a 29 cm concrete slab and 40 cm of insulation with a thermal conductivity of 0.026 W(mK)$^{-1}$. In some locations it is covered by a green roof or a terrace. Due to the low thermal conductance of 0.0625 Wm^{-2}K^{-1} of the roof, and due to the unavailability of models for a green roof or ventilated cavity, these roof covers are neglected.

Window thermal properties are determined using the glazing datasheets, which contain the glass sheet properties, cavity filling and further lists what coatings are applied. Based on this information a glazing system is created in Window 7.3 (Finlayson et al. 1993). When the exact coating is unavailable in the International Glazing Database (IGDB), a coating with a similar name and coefficients as the datasheet is used. The main properties for the glazing types are summarised in Table 8.

Most windows of floors 0 and -1 use laminated glass, i.e. types GT 402 and GT 405. For these windows the exact glazing system could not be configured in Window 7.3 because the combination of the laminated glass and coating type is not contained in the IGDB. Since a non-laminated version of the same glazing system is also used in Solarwind, and their datasheet properties differ minimally, the properties from the non-laminated version are used for both the laminated and the non-laminated glazing.

A few individual windows use fire-resistant glazing type GT 509. The coatings for these glazing types are unavailable in IGDB. Moreover these individual windows are not simulated separately. Therefore the model assumes that the thermal properties are equal to the properties of the adjacent windows.

Glazing type 60/28 is used for the glazed boxes at the north façade. Its properties are computed using the correct window coatings, but without laminated glass.

3.1.6 Internal heat gains

Following internal heat gains are considered:

- sensible heat gains from occupants,

- latent heat gains from occupants,

- sensible heat gains from lighting,

Table 9: Parameters of DHW tank and their integrated heat exchanger (HEX) models.

Parameter	Value	Source
Volume	0.5 m^3	Datasheet
Height	1.65 m	Datasheet
Insulation thickness	{15, 7, 11} mm	Calibration
Segments	4	Minimum value
HEX inlet height	1.2 m	Datasheet
HEX outlet height	0.25 m	Datasheet
Nominal HEX heat flow rate	$1.1 \cdot 33$ kW	Datasheet, calibrated
Nominal tank temperature	35 °C	Datasheet
Nominal HEX inlet temperature	70 °C	Datasheet
Nominal HEX mass flow rate	0.83 kg/s	Datasheet
HEX pipe length	25 m	Datasheet
HEX pipe cross section	5.3 cm^2	Datasheet

- sensible heat gains from appliances.

The number of occupants in each zone as a function of time is estimated using the methodology proposed by Jorissen et al. (2018a). For a description of how occupants are modelled see (Jorissen et al. 2018b). Sensible and latent heat loads of 73 W and 58 W per person are assumed based on (ASHRAE 2008). The electrical power use for lighting and appliances is measured individually for five zones per floor. These measured electrical powers are injected as heat load into the building zones. The electrical power measurements of zone 1 are attributed to its two sub-zones based on their relative floor area. I.e. 65% of the gains are injected into zone 1b. All sensible heat gains are split into a radiant and a convective part. We estimate that the LED lighting emits about 50% of the electrical power as radiant heat. The radiant fraction of electrical appliances is assumed to be 20% (ASHRAE 2008). Radiant heat is distributed over all walls as described by Jorissen et al. (2018b). Convective heat is injected into the thermal plume model.

3.2 HVAC component models

This section provides further implementation details about the used HVAC component models.

3.2.1 Borefield model

The borefield model described by Picard and Helsen (2014) is used, which uses following parameters. The borehole radius of 7.5 cm, soil thermal conductivity of 2.19 W(mK)$^{-1}$, soil volumetric heat capacity of 2200 kJm^{-3}K^{-1} are obtained from the Thermal Response Test (TRT) documentation. The double U-tube diameter of 25 mm, material and thickness of 2.9 mm are obtained from a data sheet. The thermal conductivity of the PE100 tubes is estimated to be 0.38 W(mK)$^{-1}$ based on online information of Unidelta (0.45 W(mK)$^{-1}$), iPlex (0.38 W(mK)$^{-1}$), Asahi-America (0.4 W(mK)$^{-1}$) and Ineos (0.4 - 0.49 W(mK)$^{-1}$). The grout thermal conductivity of 2.32 W(mK)$^{-1}$ and density of 1490 kgm^{-3} are obtained from the grout material datasheet. Its specific heat capacity is estimated to be the same as the one of concrete and equals 840 J(kgK)$^{-1}$. The borehole coordinates are obtained from building plans.

We further assume that all boreholes have the same average length of 29.6 m since the model does not support multiple borehole lengths. Decoupling the borefield into two parts is considered to be a worse option since then the coupling and interaction between the two borefield parts are neglected.

3.2.2 Domestic hot water tank model

Three Domestic Hot Water (DHW) tanks supply hot water to the building. The DHW tank is modelled using the `StratifiedEnhancedInternalHex` model from the buildings library. The tank dimensions and internal heat exchanger heat transfer properties are obtained from the manufacturer technical datasheet [2] and are summarised in Table 9. The heat exchanger and buoyancy dynamics were configured such that small time constants are avoided. This required `allowFlowReversal=false` since otherwise large algebraic loops are formed due to the series discretisation of the internal heat exchanger. The tank insulation thickness is calibrated using measurement data.

DHW load profiles are unavailable and therefore we assume that no domestic hot water is consumed. However, the circulation of hot water in the DHW pipes, and the corresponding heat losses, are simulated. The circulation pipe lengths are calibrated to match the observed heat losses, assuming an insulation thickness equal to the pipe radius and $k = 0.035$ W(mK)$^{-1}$. A circulation pump flow rate of 0.5 kg/s is assumed.

3.2.3 Fan and pump model

Fans and pumps are modelled using the same model, which is described in detail by Wetter (2013). The most important equations are repeated here for pumps.

The model considers a flow characteristic for pump speed $n_1(t)$ that computes the pressure difference between the pump inlet and outlet as

$$\Delta p_1(t) = f_1(\dot{V}_1(t)) \tag{43}$$

and the electric power either using a power curve

$$P_1(t) = f_2(\dot{V}_1(t)) \tag{44}$$

or a hydraulic and electrical efficiency curve such that

$$P_1(t) = f_3(\dot{V}_1(t))f_4(\dot{V}_1(t))\Delta p_1(t)\dot{V}_1(t) \tag{45}$$

where $\dot{V}_1(t)$ is the volumetric flow rate through the pump and functions $f_i(t)$ are implemented using piecewise cubic splines. These equations are however only valid for speed n_1. Affinity laws are therefore used to compute the pressure difference and electrical power at other speeds $n_2(t)$. The actual pump pressure difference $\Delta p_2(t)$, volumetric flow rate $\dot{V}_2(t)$ are thus computed from pressure curve (43) and affinity law equations

$$\frac{\dot{V}_2(t)}{\dot{V}_1(t)} = \frac{n_2(t)}{n_1}, \tag{46}$$

$$\frac{\Delta p_2(t)}{\Delta p_1(t)} = \left(\frac{n_2(t)}{n_1}\right)^2. \tag{47}$$

The electrical power $P_2(t)$ is either computed from the power curve (44) and affinity law equation

$$\frac{P_2(t)}{P_1(t)} = \left(\frac{n_2(t)}{n_1}\right)^3, \tag{48}$$

or using

$$P_2(t) = \Delta p_2(t)\dot{V}_2(t)f_3\left(\dot{V}_2(t)\frac{n_1}{n_2(t)}\right)f_4\left(\dot{V}_2(t)\frac{n_1}{n_2(t)}\right). \tag{49}$$

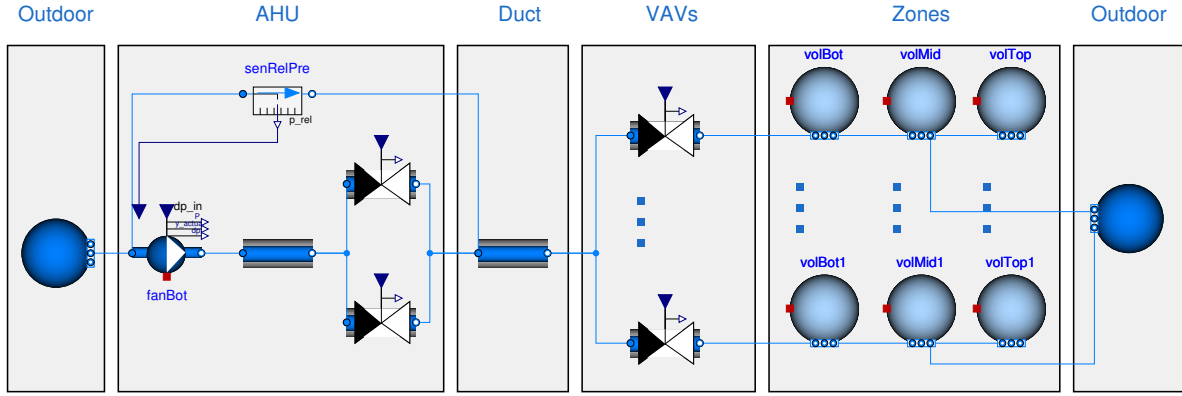[2]Vitocell-V 100 Technical Data, 500 l

Figure 8: Schematic of the supply side of the air flow model of one of the two AHUs.

All pump models use these equations to compute the flow rate, pressure difference and electrical power use. Pump types are obtained from Figure 3. Based on these types, the models are parametrised by sampling the flow curve and the power curve that are typically supplied in manufacturer data sheets. The resulting pump curves are added to the IBPSA library. Pumps that prescribe a fixed head or pressure difference, do not need these equations to determine the pressure difference or the flow rate, but they are required to compute the electrical power use.

For fixed differential pressure pumps, the pressure set point is obtained through visual inspection of the pump.

3.2.4 Air flow network

Jorissen et al. (2018c) explain how the hydronic system models were configured such that only simple algebraic loops are generated, which contain only few equations and, more importantly, few iteration variables. Similarly, we now discuss how the air flow network is configured such that again only simple algebraic loops are formed.

A schematic of the complete air flow model, which contains components from multiple HVAC component models, is shown in Figure 8. The model is bounded at both sides by the fixed outdoor pressure. The AHU consists of a fan, the lumped pressure drop of components with a fixed flow coefficient and two dampers. The main supply duct is modelled using a pressure drop component with a fixed flow coefficient. VAVs are modelled using a pressure independent damper model, which is described in more detail by Jorissen et al. (2017). Zones are modelled using three volumes that cause no pressure drop. All pressure drops within one branch of the flow network are merged into a single equation, as described by Jorissen et al. (2018c). E.g. the variable flow coefficient of a damper and the fixed flow coefficient of the duct contraction in series with the damper are combined into a single pressure drop equation.

The illustrated flow network is modelled using quasi-stationary equations, which generate an algebraic loop. Algebraic loops are solved in Dymola by choosing a number of iteration variables from which residual equations are evaluated. The residual equations are iteratively solved using a Newton solver such that the equation values converge to zero. In general, the fewer iteration variables that are used, the lower the computation cost for this algorithm. In the drawn configuration only three iteration variables are required: the pressure at both sides of the dampers, and the pressure at the duct outlet (right). Indeed, the zone air volume pressures and the fan inlet pressure are known and equal to the outdoor pressure. The fan outlet pressure equals the inlet pressure plus the prescribed pressure difference set point. From these pressures all mass flow rates can be computed. This number of iteration variables is acceptable, but can be improved further since the fan has a supply duct

pressure difference set point, instead of a fan outlet pressure difference set point.

This is modelled by including relative pressure sensor `senRelPre`. Its two ports are connected to the fan inlet and the duct inlet. The measured differential pressure output is connected to a fan input. Then the fan model is changed such that it prescribes the relative pressure *input* instead of the pressure difference between the fan inlet and outlet. Since the fan inlet pressure is known and equal to the boundary pressure p_{amb}, Dymola thus computes duct inlet pressure from the known boundary value and the prescribed pressure difference of the fan. Since the duct inlet pressure is now known, one iteration variable for the duct outlet pressures is sufficient to solve the flow rates through the VAVs and the main ducts. Due to conservation of mass, the total mass flow rate of the VAVs also passes through the AHU and therefore only one iteration variable is required. This results in two algebraic loops with one iteration variable instead of one algebraic loop with 3 iteration variables. The described functionality for prescribing relative pressures has been made available in the IBPSA library as parameter option of the `FlowControlled_dp` model.

3.2.5 Heat exchanger models

The VAV and AHU heating coils are cross flow heat exchangers and the solar collector, pellet furnace and heat pump heat exchangers are counter flow heat exchangers. The ϵ-NTU method is used to model these heat exchangers.

According to Kays and London (1964), the heat exchange effectiveness of counter flow heat exchangers equals

$$\text{NTU}(t) = \frac{\text{UA}}{C_{min}(t)} \tag{50}$$

$$\epsilon(t) = \frac{1 - \exp\left[-\text{NTU}(t)(1 - C^*(t))\right]}{1 - C^*(t)\exp\left[-\text{NTU}(t)(1 - C^*(t))\right]} \tag{51}$$

$$\dot{Q}(t) = \epsilon C_{min}(t)\Delta T_{in}(t) \tag{52}$$

where NTU is the number of transfer units, UA is the heat conductance of the heat exchanger, $C^*(t)$ is the heat capacity ratio, $\Delta T_{in}(t)$ is the temperature difference between the heat exchanger inlets, $C_{min}(t)$ is the lowest of the two heat capacity rates and $\dot{Q}(t)$ is the heat flow rate between the two fluids.

For counter-flow heat exchangers equation

$$\epsilon(t) = 1 - \exp\left(\frac{\exp\left(-C^*(t)\text{NTU(t)}^{0.78}\right) - 1}{C^*(t)\text{NTU(t)}^{-0.22}}\right);$$

from Bergman et al. (2011) is used.

These equations are however modified such that zero flow rates do not lead to a division by zero.

The UA value of each counter-flow heat exchanger is computed as

$$\text{UA} = \dot{Q}_{nom}/\text{LMTD} \tag{53}$$

where $\dot{Q}_{nom}$ is the nominal data sheet heat flow rate and LMTD is the logarithmic mean temperature difference corresponding to this heat flow rate. The model thermal power at nominal operating conditions is verified to match the data sheet. For the Trox WT 160 TVZ cross flow VAV heating coils, the UA value is computed such that the model matches manufacturer performance data for the system nominal flow rate. The used UA values are summarised in Table 10. UA values are constant, which implies that the flow rate dependency of convective heat transfer coefficients is neglected.

29

Table 10: Manufacturer data of the heat exchangers. The reported UA values are computed from the other data. For the furnace, the UA value is increased by a factor 1.5 to better match the measurements. Indices 1 are used to report values for the hot fluid. Note that these fluids are either water, air, or a glycol solution.

HEX	UA [W/K]	$\dot{Q}$ [kW]	$\dot{m}_1$ [kg/s]	$\dot{m}_2$ [kg/s]	$T_{in,1}$ [°C]	$T_{in,2}$ [°C]	$T_{out,1}$ [°C]	$T_{out,2}$ [°C]	LMTD [K]	Source Datasheet
Summer	69 060	240	14.3	19.1	21	14	17	17	3.5	Alfa laval
Winter	44 000	110	13.1	9.45	6	1	4	4	2.5	Alfa laval
Furnace	$1.5 \cdot 5000$	100	1.21	1.2	90	50	70	70	20	Alfa laval
Solar	4170	60	0.4	0.47	80	30	40	60	14.4	Alfa laval
VAV coil	120	2.53	0.06	0.2	50	16	40	28.3	NA	Trox

3.2.6 Pellet Furnace

Only the unit weight, dimensions and nominal thermal power of the pellet furnace are available. Therefore, the furnace thermal model is simple and does not compute the unit efficiency. The main characteristics of the furnace's internal controller are derived from measurement data.

When the unit is activated, thermal power is injected into an internal water buffer of 160 l. The furnace thermal power equals

$$\dot{Q}_f(t) = c\dot{Q}_{f,nom}\mathrm{mod}(t) \tag{54}$$

where $c = 0.85$ is a fixed correction coefficient, $\dot{Q}_{f,nom} = 100$ kW is the nominal thermal power and mod(t) is a modulation coefficient that limits the unit outlet temperature to 87 °C. The unit is activated by an external control signal. The unit then stays on for a minimum of 2 hours. When the unit is deactivated, it stays off for a minimum of 2 hours. Thermal power is only delivered to the water tank after a starting period of 15 minutes. The unit has an output that requests an external circulation pump to be activated when the buffer water temperature exceeds 65 °C. A second output indicates whether the unit has completed its minimum on period.

3.3 Control

The BMS control strategy is described in Section 2.3. Its implementation primarily involves the mapping of control blocks and the connections from the control strategy into their Modelica counterparts. For many components this is trivial. However, some control blocks have options that do not exist in typical Modelica implementations, or their implementation is unknown. These components are discussed here. Most component parameter values are not reported since there are a few thousand of them.

3.3.1 PI controller model

PI controllers are used extensively in the BMS. The Annex 60 library (Wetter et al. 2015) (IBPSA library) has a PID controller model. When configured as a PI controller, it computes the control signal $y(t)$ based on a set point input $u_{set}(t)$ and measurement input $u_m(t)$ as

$$y(t) = \min(y_{max}, \max[y_{min}, y_{PI}(t)]) \tag{55}$$

$$y_{PI}(t) = k[u_{set}(t) - u_m(t) + I(t)] \tag{56}$$

$$\frac{\mathrm{d}I(t)}{\mathrm{d}t} = \frac{u_{set}(t) - u_m(t) - \mathrm{aw}(t)}{T_I} \tag{57}$$

$$\mathrm{aw}(t) = \frac{y(t) - y_{PI}(t)}{0.9k} \tag{58}$$

where y_{max} and y_{min} are the upper bound and lower bound of the output, k is the PI controller gain, T_I is the integrator time constant, which is usually 180 seconds, and $aw(t)$ is the output of the anti-windup implementation that limits the integrator value.

This PI controller implementation is insufficiently detailed to model the BMS PI controller since the model:

1. cannot model time-dependent gains k,

2. cannot model time-dependent bounds y_{max} and y_{min},

3. has a different anti-windup implementation than the BMS,

4. cannot bound $\frac{\mathrm{d}y(t)}{\mathrm{d}t}$, the rate of change of the output.

For these reasons a new PI controller model is developed. Some implementation aspects of the model are discussed here.

The BMS PI controller allows to define an upper bound and lower bound for the time derivative of the controller output, such that

$$y_{d,min} \leq \frac{\mathrm{d}y(t)}{\mathrm{d}t} \leq y_{d,max}. \tag{59}$$

This could be implemented in Modelica using

$$\frac{\mathrm{d}y_{d,lim}(t)}{\mathrm{d}t} = \min\left(y_{d,max}, \max\left[y_{d,min}, \frac{\mathrm{d}y_{PI}(t)}{\mathrm{d}t}\right]\right), \tag{60}$$

$$y(t) = \min(y_{max}, \max\left[y_{min}, y_{d,lim}(t)\right]). \tag{61}$$

However, such an implementation would sustain a constant difference between the values of $y_{d,lim}(t)$ and $y_{PI}(t)$ after the activation of one of the rate of change bounds. Solving this would require a second anti-windup implementation. Moreover, the computation of $\frac{\mathrm{d}y_{PI}(t)}{\mathrm{d}t}$ in Modelica would involve the computation of

$$\frac{\mathrm{d}y_{PI}(t)}{\mathrm{d}t} = k\left(\frac{\mathrm{d}u_{set}(t)}{\mathrm{d}t} - \frac{\mathrm{d}u_m(t)}{\mathrm{d}t} + \frac{u_{set}(t) - u_m(t) - aw(t)}{T_I}\right). \tag{62}$$

The set point $u_{set}(t)$ is often computed using discrete logic and therefore $\frac{\mathrm{d}u_{set}(t)}{\mathrm{d}t}$ may be undefined, e.g. when instantly switching between the outputs of two heating curves. Dymola therefore does not accept equation (62), and the rate limiter output $y_{d,lim}(t)$ is computed approximately from

$$\frac{\mathrm{d}y_{d,lim}(t)}{\mathrm{d}t} = \min\left(y_{d,max}, \max\left[y_{d,min}, \frac{y_{PI}(t) - y_{d,lim}(t) + aw_d(t)}{\tau_{d,lim}}\right]\right) \tag{63}$$

$$aw_d(t) = y(t) - y_{d,lim}(t) \tag{64}$$

where $\tau_{d,lim}$ is a time constant that determines the time delay of the computation. Variable $aw_d(t)$ is an anti-windup implementation that limits how much $y_{d,lim}(t)$ can rise above or below $y_{max}(t)$ and $y_{min}(t)$ when these bounds are active. This mitigates big jumps in the output of $y(t)$ when the regular output limit is active and the bound value $y_{min}(t)$ or $y_{max}(t)$ is then suddenly relaxed by the BMS.

The anti-windup implementation of the regular output limits is also implemented different from (58), since this implementation can also create an output overshoot when $y_{min}(t)$ or $y_{max}(t)$ changes quickly. The integrator output derivative $I(t)$ is penalised such that

$$-\Delta I_{max} \leq y(t) - k\left[u_{set}(t) - u_m(t) + I(t)\right] \leq \Delta I_{max} \tag{65}$$

is satisfied, where the middle term is formed by moving all terms in (55) and (56) to one side, which returns zero unless a bound is active, and ΔI_{max} is an integrator saturation limit, which is a parameter of the PI controller. The integrator output is computed using a differential equation that contains a penalty term when inequality (65) is not satisfied. The larger the gain of this penalty term, the more accurate the result is, but the smaller the model time constants.

3.3.2 Heat pump cascade

The BMS heat pump controller consists of 8 PI controllers that are activated in sequence. When a PI controller output reaches 100 % the next PI controller in the sequence is activated, and the output of the former PI controller is fixed to 100 % until the next PI controller output drops to 0 %. A cascade consisting of 8 stages is thus formed. The cascade implementation requires PI controller concepts, such as blocking its output value based on an external signal, that are not available in Modelica. Moreover, the exact implementation is unknown.

Therefore, this control sequence is implemented in a simplified and more intuitive way by considering a single PI controller of which the output is bounded by 0 and 8. The outputs of eight hysteresis controllers become high when the PI controller output exceeds $\{1, 2, 3, 4, 5, 6, 7, 7.99\}$ and become low when it is less than $\{0.01, 1, 2, 3, 4, 5, 6, 7\}$. The last hysteresis controller in the cascade with a high output determines which heat pumps are activated at that point in time. For subsequent stages in the cascade, the number and type of heat pumps are selected such that the total thermal power equals $\{29, 43, 58, 72, 86, 101, 115, 144\}$ kW. This leads to an implementation that result in very similar controller behaviour, but with less complexity.

3.3.3 Other

Other custom components that have been implemented are a set-reset (SR) flip-flop *with dominant set*, simple blocks such as integer equality comparisons and switches, a minimum on block that maintains a high signal at the output for a minimum period when the input becomes high, an off delay block that maintains a high signal at the output for a minimum period when the input becomes low, and a block that returns the maximum value of a number of inputs at its output and further returns the index of the highest input.

4   Verifications

This section presents verifications additional to the ones presented in the paper. As in the paper, we first describe the system part that is verified and what measured boundary conditions are applied. Then results are presented and discussed.

4.1   VAV heating coil subcircuit

The VAV heating coil subcircuit is verified by modelling all VAVs, including heating coils and their heating coil two-way valves. This includes heating coil valves of floor -1, for which the exact system layout is not documented. The valves are connected in parallel to a pipe that is connected to a pump with a fixed head of 6 m. The pump control signal and the control signals of all two-way valves are model boundary conditions.

The total heating coil mass flow rate is measured using a heat meter. Figure 9 compares the measured with the simulated flow rate. When many valves are fully opened, typically at the start of a day, the flow rate error can become large. This error is not observed when many valves are only partly opened. The cause for this can be that the flow network pressure drops are not modelled up to the detail of individual pipes and calibration valves, and therefore the model is only accurate when the valve pressure drops dominate.
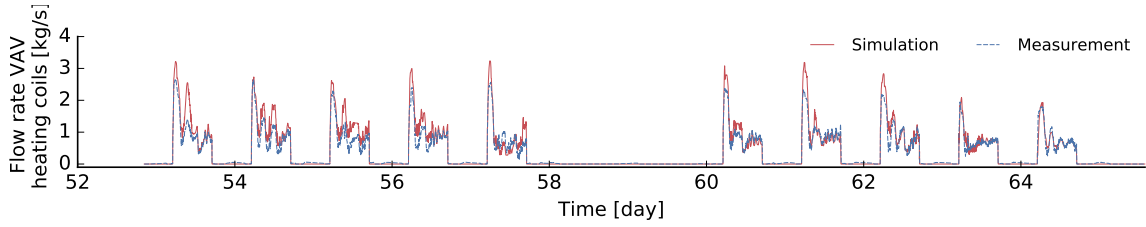
Figure 9: Verification of total mass flow rate for VAV heating coils.

We conclude that errors in the flow network model cause an overprediction of the peak heating capacity of the VAV heating coils. However, the closed-loop controller partly compensate for this since they track a fixed supply temperature set point. This model error should therefore not introduce large errors in the computation of the building energy use.

4.2 Controller

Many parts of the controller are verified, of which the most important results are reported here. Temperature sensor measurements, the RMAOT, AHU three-way valve openings and on/off control signals, and the pellet furnace pump demand signal are used as model boundary conditions. Some measurements that are required for verifying the VAV controller are not logged due to the BMS measurement limit. This controller is therefore not verified separately.

Results are presented in Figure 10. The left subgraphs show a spring period when the furnace is used. The right subgraphs show a summer period when the solar collectors are used and when the CCA switches between heating and cooling mode. The first subgraph shows the inputs of the PI controller that controls the furnace supply water inlet temperature using the installed three-way valve. The measured and simulated valve openings are shown in the second subgraph. A large error is observed. Since the PI controller inputs are measured, this error suggests that the Modelica implementation of the PI controller is not sufficiently accurate. The algorithms of the real PI controller implementation are however unavailable, such that the error is hard to pinpoint. The mismatch may also be caused by the limited accuracy of the measurement data. These mismatches cause the 70 % valve opening threshold of the furnace not to be crossed, due to which the furnace does not enter a Tmax mode. This causes many errors in the furnace mode that is displayed in the third subgraph.

An error that is unexplained by this is the transition from furnace mode 8 to mode 7 around day 117.5 and 118.25. This error is caused by a different measurement inaccuracy: due to the measurement update threshold and averaging of the measurements, the measurements tend to lag behind their real values. When a DHW tank temperature becomes low, it will trigger a heat demand, which relatively quickly increases the tank temperature. Due to this quick feedback loop, the temperature threshold is sometimes not crossed in the simulations, due to which no heat demand is generated, which affects the system modes.

These measurement inaccuracies also affect the HWST mode since there is a feedback from the furnace mode into the HWST mode. Errors in the solar mode are caused by mismatching modes of the HWST or measurement errors. E.g. the error around day 117.3 and 118.3 is caused by the wrong value of the HWST mode. The error around day 117.75 is caused by a solar collector temperature measurement that does not drop below a threshold, after which the solar collector temperature increases. At day 118.6 both errors occur. During the summer period no noticeable errors are observed.

The seventh subgraph shows the CCA mode. The mode is well predicted except on day 183. The RMAOT temperatures that are shown in the sixth subgraph however suggest that a manual override occurred in the building since the outdoor temperatures are higher than the days before and therefore the cooling mode should be activated also during day 183. At day 174 and day 176, the simulation predicts a mode change which does not occur in practice. This may be caused by a
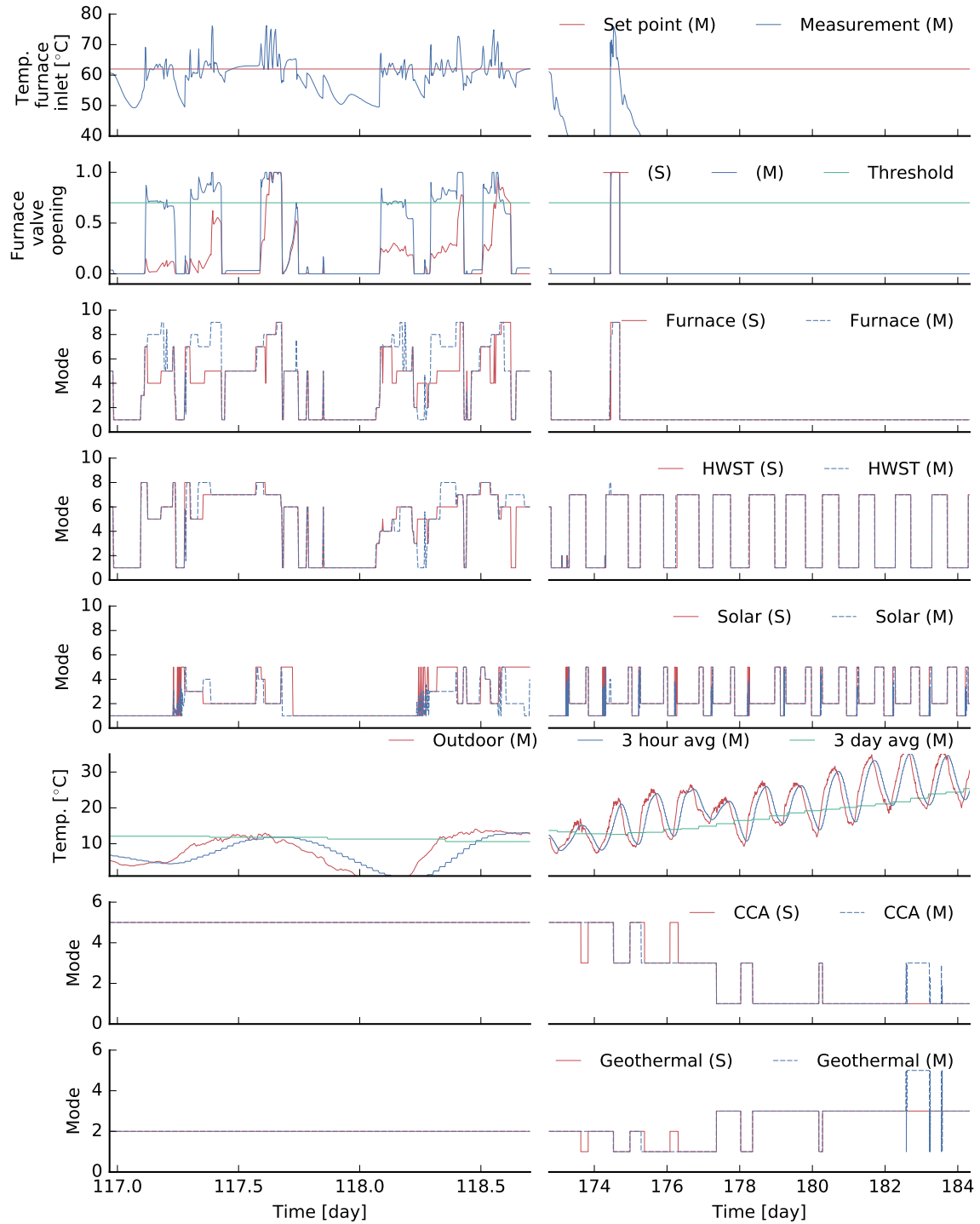
Figure 10: Verification of the main control model modes. A selection of boundary conditions is illustrated in the first and the sixth plots.
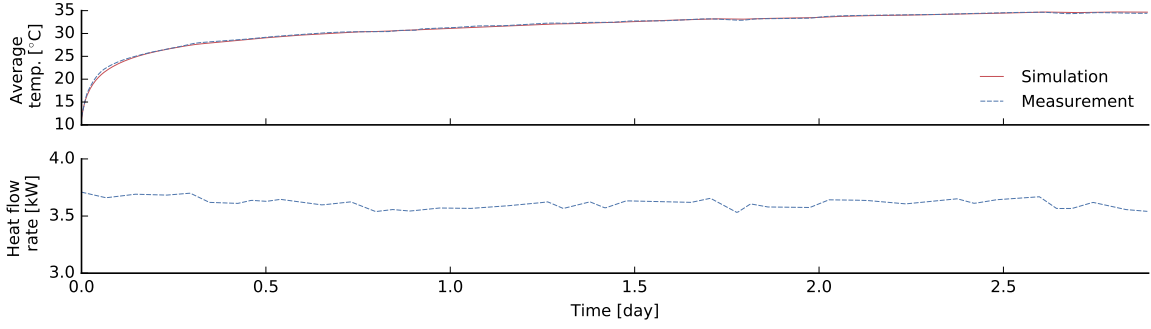
Figure 11: Verification of borefield model using thermal response test.

wrong parametrisation of the outdoor temperature thresholds, which can be changed manually by the building operator and which are fixed in this verification based on observations at a different point in time.

The last subgraph shows the geothermal borefield modes, which are clearly computed from the CCA modes.

Based on these modes, the valve openings and pump control signals are computed. These results were also verified but are not part of the scope of this text.

We conclude that, although some errors occur, these can typically be explained by measurement inaccuracies or the absence of system feedback. The controller model is thus a good representation of the real BMS.

4.3 Borefield

The borefield model is verified using measurements from a Thermal Response Test (TRT) of a single borehole and using measurements during operation.

During the TRT a thermal power of about 3.6 kW was injected in the borehole. The TRT borehole temperature was measured in June 2009 to determine the undisturbed ground temperature of 11.28 °C. The initial ground temperature is assumed to be uniform and equal to this measured value. The borehole pipe shank spacing is unknown and is calibrated based on the TRT. The mean of the inlet and outlet temperatures of the borehole is compared with the measured average in Figure 11. This verification shows good results, partly due to the calibration of the borehole pipe shank spacing.

The borefield model is further verified using measurements from a heat meter. The borefield and a pump are modelled. The pump flow rate equals 1.225 m^{3}h^{-1}. The measured thermal power is injected into the borefield. The verification period consists of over 500 days and starts on May 2014. A uniform initial ground temperature of 13 °C is assumed.

The response of the borefield is shown in Figure 12. The measured inlet and outlet temperatures of the borefield are compared with the simulated ones in the first subgraph. The second subgraph compares two temperature measurements at the top and bottom of the borefield, with the value of model variable `TWall`, which represents the boundary temperature between the short and the long term response of the model. The exact location of the sensors is unknown so they may not be directly comparable to `TWall`. The pump mass flow rate and measured heat flow rate are displayed in the bottom graphs. Two cooling periods are used to verify the model due to the high variability of the heat flow rates during heating periods, which makes it visually difficult to compare results and since pipe thermal dynamics affect the measured temperatures.
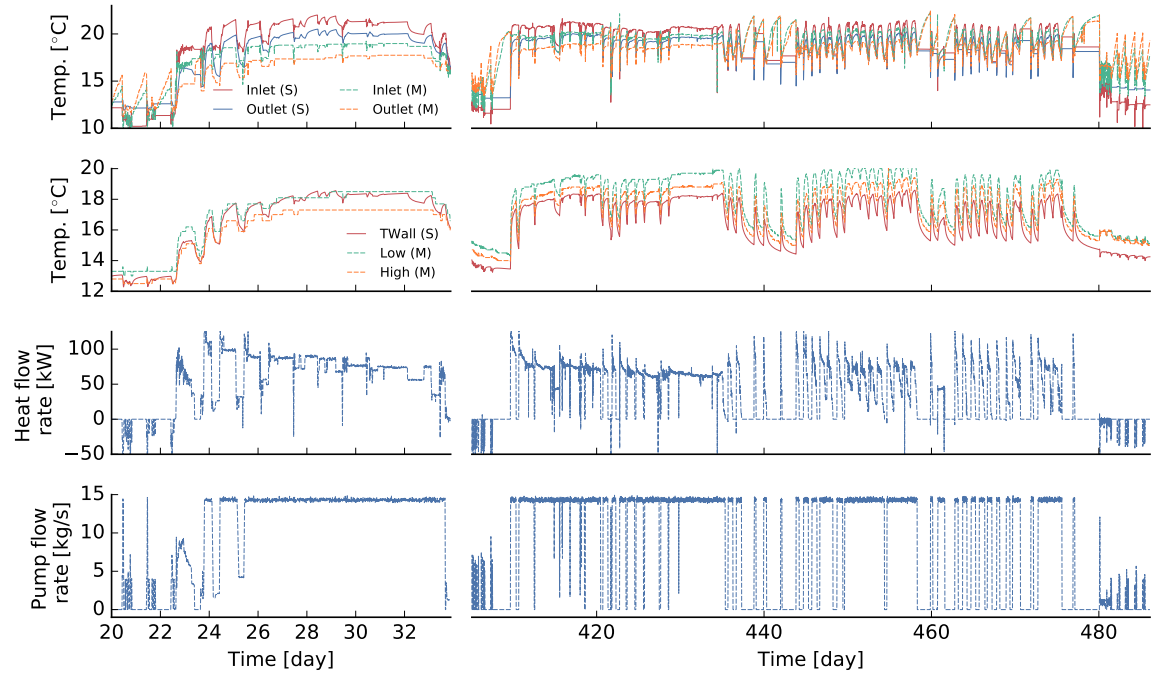
35

Figure 12: Verification of the borefield model. The first subgraph compares measured with simulated inlet and outlet temperatures of the borefield. The second subgraph compares temperatures inside the borefield. The remaining graphs are boundary conditions. The third graph shows the thermal power that is injected. The last subgraph shows the pump mass flow rate.
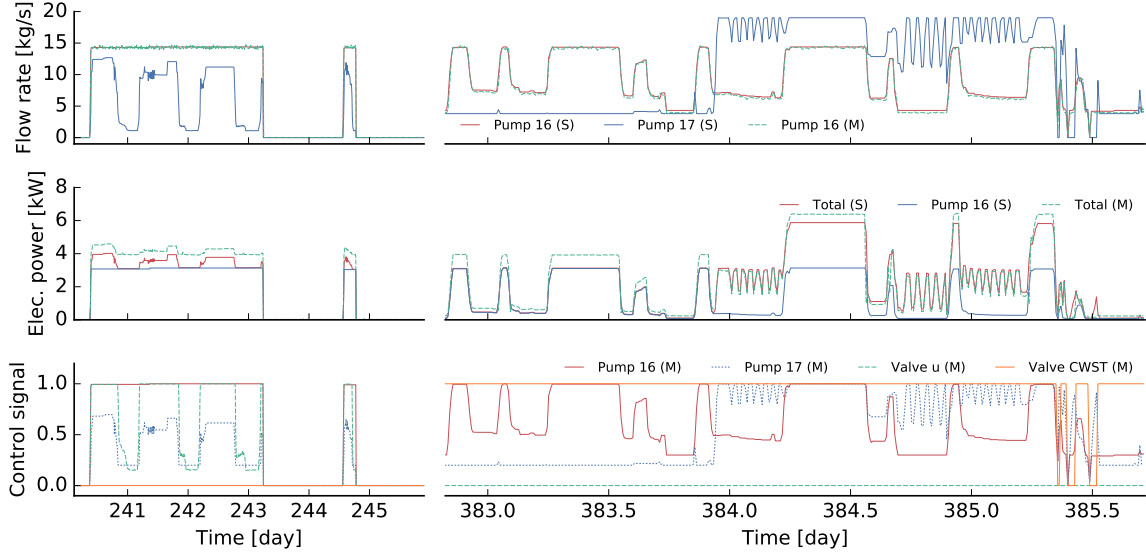
Figure 13: Verification of the mass flow rate of two main circulation pumps in subgraph 1 and the electrical power use in subgraph 2 for the control signals in subgraph 3.

The first period shows that the borefield core temperature is correctly predicted at the start of the verification period for the initial ground temperature of 13 °C. However, the borefield inlet and outlet temperatures are overpredicted, suggesting that the borehole thermal resistance is overpredicted, or that the model initial conditions are not accurate enough. Furthermore, the simulated temperatures fluctuate more strongly than the measurements. This is caused by the measurement accuracy during this period. A temperature threshold of 0.5 K was used for logging the borefield temperatures. When the threshold is crossed, this leads to a discrete change in the computed heat flow rate, even though the heat flow rate changes smoothly in reality. This can be seen in the third subgraph and by the fluctuations caused.

The second part of Figure 12 occurs 400 days later. Borefield measurements were then logged each minute, such that a smoother heat flow rate is observed. The second subgraph shows that a drift in the borefield core temperature has occurred, which is now underpredicted by about 1 K. This can be caused by model approximations, by an overestimation of the ground thermal conductivity or volumetric heat capacity, or by an underestimation of the undisturbed ground temperature. The response to discrete changes in thermal power is however well predicted. Despite the underprediction of the ground temperature, the borefield inlet and outlet temperatures are overpredicted.

We conclude that the borefield model has both long-term and short-term model errors up to a few Kelvin. This can cause small errors in the computation of the heat pump COP, but more importantly it can cause an underprediction of the passive cooling capacity of the borefield. The model simulations are thus on the conservative side with respect to this effect.

4.4 Pump electrical power use

The pump models are verified using electrical power measurements from the two largest pumps. The borefield circulation pump (pump 16 in Figure 3), the passive cooling circulation pump (pump 17 in Figure 3) and its two-way valves (valve u in Figure 3 and the valve connection to the Cold Water Storage Tank (CWST)) are simulated. The pressure drop in each of the three circuit branches is modelled using a pressure drop component with a fixed flow coefficient, which is calibrated using the
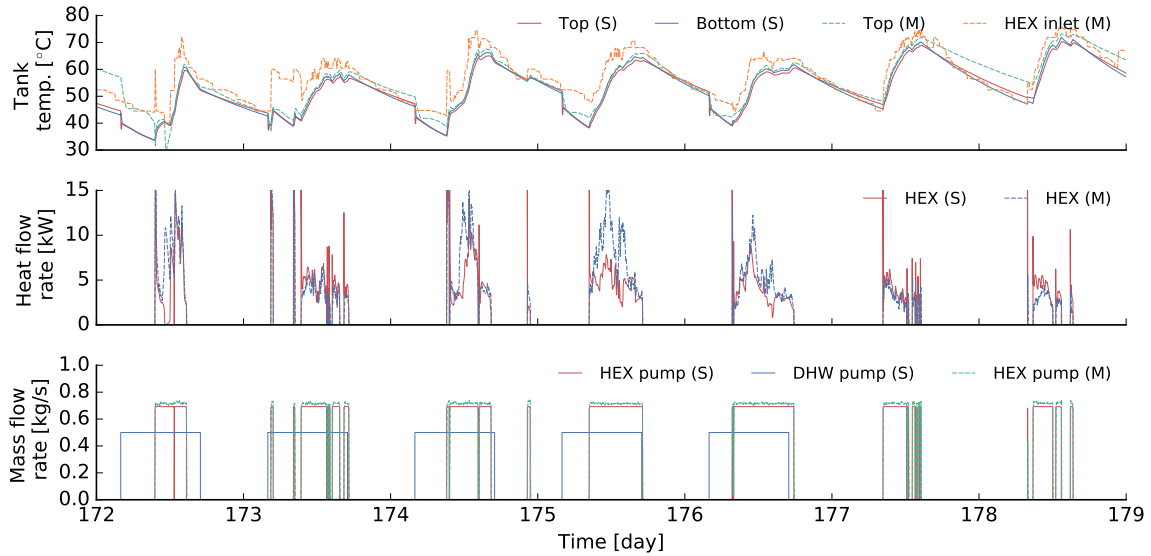
Figure 14: Verification of DHW tanks. The first two subgraphs compare the simulated tank temperatures and heat flow rates to measurements. The last subgraph shows boundary conditions of the verification.

measurement data. The measured pump and valve control signals are boundary conditions.

The first subgraph in Figure 13 compares the measured flow rate of pump 16 with the simulated flow rate. The nominal pressure drop of the circuit is calibrated to 165 kPa using measurement data from the first period. The second period shows that the model is also accurate for other pump control signals. During the first period the active electrical power use is underpredicted by about 20 %. When both pumps are at nominal speed, around day 384.5, the error is only 9%, which can be explained by the fact that the efficiency of the frequency converter is not taken into account. Experiments have shown that the electrical power use of pump 17 at 20 % of the nominal speed equals 250 W, whereas the simulation predicts a power use of only 25 W. Indeed, the affinity laws do not consider zero load losses of electrical motors, which can dominate for low speeds. The pump model accuracy could thus be improved. Further errors may be caused by the fact that the frequency converter of pump 17 performs a non-linear mapping of the control signal to the pump speed, which was not taken into account since the curve shape is not well known.

We conclude that the pump models are sufficiently accurate when the nominal circuit pressure drop is calibrated properly. Improvements could be made to the way how frequency converters and part load operation of motors is modelled.

4.5 Domestic hot water tanks

The DHW tanks are verified using a model that consists of the three tanks, three three-way valves, three pumps that supply hot water to the integrated heat exchanger, and three pumps that draw water from the tanks and circulate it through the building pipes. Boundary conditions are the supply temperature at the three-way valve inlets and the control signals of pumps and valves.

Figure 14 compares simulation results for one of the three tanks during a period of one week. The model assumes that no DHW is used since DHW profiles are unknown. Verification is therefore difficult unless the DHW use is indeed zero, which is probably the case during weekends and holidays. The second day in Figure 14 is Luxembourg's national day and the sixth and seventh days are weekend days and are used to verify the model. During these days the tank thermal charging power is usually

38

Table 11: Comparison of heating (h), cooling (c) or electrical (el) energy use [MWh] of i) the building envelope verification that uses measured boundary conditions ('Envelope'), ii) the building model including HVAC and controls ('Building') and iii) measurement data ('Measurement'), for north (N) and south (S) CCA circuits, east (E) and west (W) air handling units and the VAV heating coils. *Ven* denotes the cooling energy that corresponds to the sum of the enthalpy flow rates of AHU1, AHU2, and any air infiltration or exfiltration that compensates for supply and return flow rate imbalances. The energy uses are in MWh for a year starting on February 1st 2015.

	$CCA_{N,h}$	$CCA_{N,c}$	$CCA_{S,h}$	$CCA_{S,c}$	VAV	$AHU_{E,el}$	$AHU_{W,el}$	Ven
Envelope	31.8	25.4	30.5	19.5	35.1	NA	NA	169
Building	19.3	31.1	24.8	29.4	21.6	18.8	19.1	177
Measurement	45.1	40.9	25.2	46.3	32.4	24.2	23.2	177

predicted correctly with errors up to 20 % for the first two days and up to 50 % for the third day. The larger error during the third day is consistent with the larger tank temperature measurement that is observed in the top subgraph. The larger initial temperature indeed results in a lower charging thermal power. The insulation thickness of the tank is calibrated such that the temperature decay of the tank is correctly predicted when the DHW circulation pump is off. The resulting thickness is 7 mm (see also Table 9) for the tank for which results are shown in Figure 14, which is considered small. This computation uses the default tank insulation thermal conductivity of 0.04 $W(mK)^{-1}$. This corresponds to a heat loss that is 7 times larger than the value reported in the datasheet. One possible explanation for this is that the hot water in the circulation pipes causes a natural buoyancy effect that maintains a small flow rate even when the circulation pump is off. To explain the additional heat loss of about 500 W, a buoyancy-induced mass flow rate of about 3 g/s would be required, which we consider a realistic flow rate.

The DHW circulation pipe length is also calibrated. For this calibration we use the fact that the water in the pipes cools down at night. When the circulation pump is enabled, this causes a large amount of cold water (26 °C) to enter the tank, which causes a temperature drop. The pipe length is calibrated such that this temperature drop is predicted correctly. This leads to large pipe lengths of {230, 230, 170} m when using a pipe diameter of 25 mm. In practice the HVAC plans indicate that the supply and return pipe respectively have a diameter of 20 mm and 32 mm. Pipe heat losses are computed assuming an insulation thickness of 15 mm and a thermal conductivity of 0.035 $W(mK)^{-1}$. The used calibration possibly overpredicts the pipe lengths if the storage tank is not well mixed, as the model implicitly assumes.

During the other days, the DHW use is clearly larger since more thermal power is used. However, standby losses amount to a significant fraction of the total energy use.

4.6 Conservation of energy

The verification of the building envelope model in the paper reveals that both the simulated CCA cooling energy use, and the heating energy use, are underpredicted. These results are repeated in Table 11. This section presents an energy balance of the building envelope that verifies conservation of energy and that allows better analysis of the energy use deficit.

For this analysis all mass and energy flow rates that enter the building are grouped and their corresponding energy flow rates are integrated as a function of time to obtain cumulative values. Figure 15 shows the integrated energy use as a function of time where

- $E_{cca,i}$ are the energy uses for the north (N) and south (S) CCA circuits for cooling (c) and heating (h),

- E_{sol} are the diffuse and direct shortwave radiative heat gains through windows,

- E_{occ} are the sensible heat gains from occupants,

- E_{int} are the internal heat gains from electrical appliances and lighting,

- E_{VAV} are the heat gains from the VAV heating coils,

- $E_{air,0-3}$ are the total (sensible *and latent*) heat losses and heat gains of floors 0–3 that are caused by mechanical ventilation,

- $E_{air,-1}$ are the total (sensible *and latent*) heat losses and heat gains of floor -1 that are caused by mechanical ventilation,

- E_{pip} are the heat losses and heat gains of the CCA pipes.

The remaining terms of the energy balance are the latent heat gains from occupants, building envelope infiltration losses, and thermal losses and gains through windows and the façade. They are included in E_{env}.

The first subgraph of Figure 15 shows that the building heat gains are dominated by the internal gains and the solar heat gains. The heat delivered by the CCA is relatively small.

The second subgraph of Figure 15 shows that this heat is primarily cooled away by the two AHUs of floors 0 – 3. However during CCA cooling mode, this cooling load is partly taken over by the CCA. We compute that the CCA cools 36 MWh during the summer period where the two main AHUs cool only 24 MWh. Building envelope heat losses are positive during winter and negative during summer.

The third subgraph confirms that the sum of these thermal power integrals equals the internal energy of the building envelope[3], which equals the sum of the internal energies of all heat capacitors and fluid volumes in the model. Energy is therefore conserved by the building envelope model. This rules out some major modelling errors.

Figure 16 further presents time series data that corresponds to the top and bottom rows of Table 11. It shows an underprediction of the south CCA heating energy use at the start of the period, and an overprediction at the end of the period. Both periods occur during winter, but the second period has much less solar irradiation. The heating energy use of the north zone is strongly underpredicted, but now especially during the first heating period. The cooling energy of both CCA zones is significantly underpredicted, although the cooling provided by the AHUs is correctly predicted. This suggests the existence of an unmodelled or underpredicted heat source. The overall results suggest that the building envelope heat losses are larger than predicted and that solar heat gains during summer are larger than predicted. However, no physical explanation for this could be identified.

Occupant behaviour such as the opening of windows and measurement errors are other possible causes for the wrong predictions. However, no proof could be found that these aspects would lead to such a substantial impact.

5   Conclusion

This document provides more detailed information about the Solarwind building, including a extensive description of the building controller. It further presents an implementation of the under-floor air distribution model, the approximate inverse Perez model, the CCA floor model, fan and pump models, the air flow network, heat exchanger models, the PI controller model and other control components. Finally, additional model verifications are presented of the VAV heating coil circuit, the controller model, the borefield model, the pump model, and the DHW storage tank model. More detailed information about the building energy use is provided in an attempt to explain the model energy use mismatch. However, no clear cause for the mismatch could be identified.

---

[3]The internal energy is computed as a sum of the internal energies of *all* components. The open-source nature of Modelica libraries was required here to obtain this internal energy for all component models.
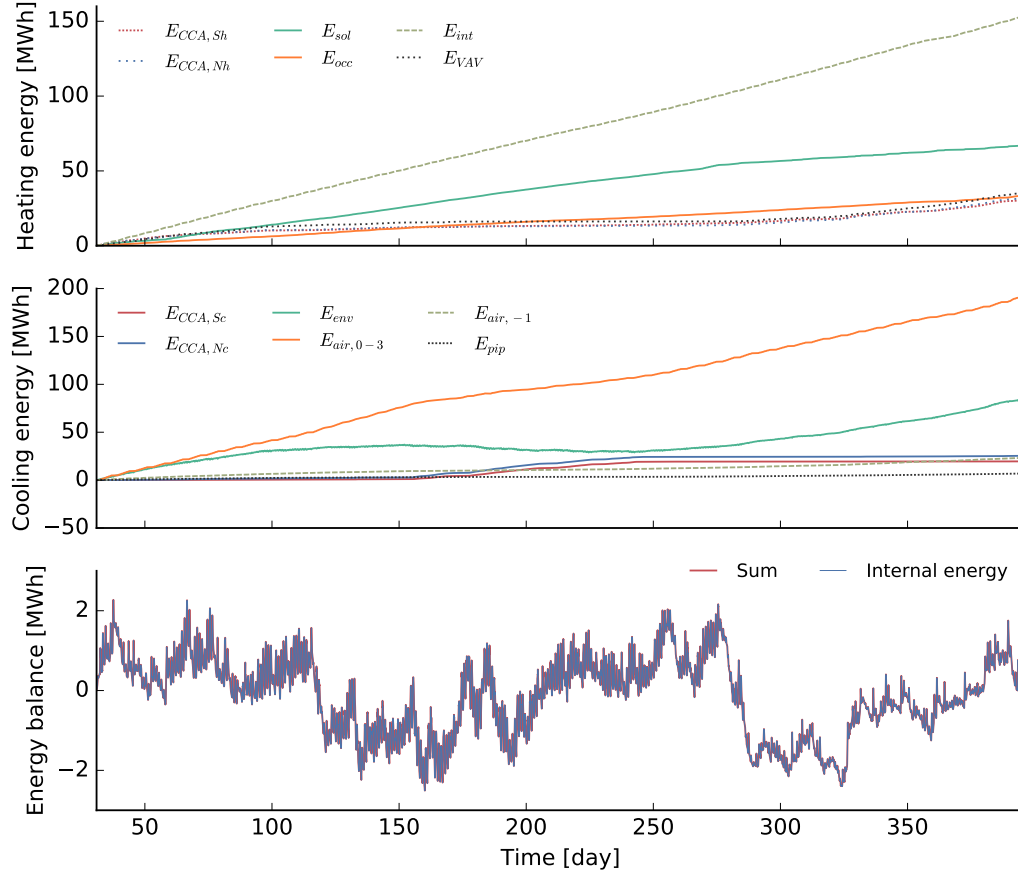
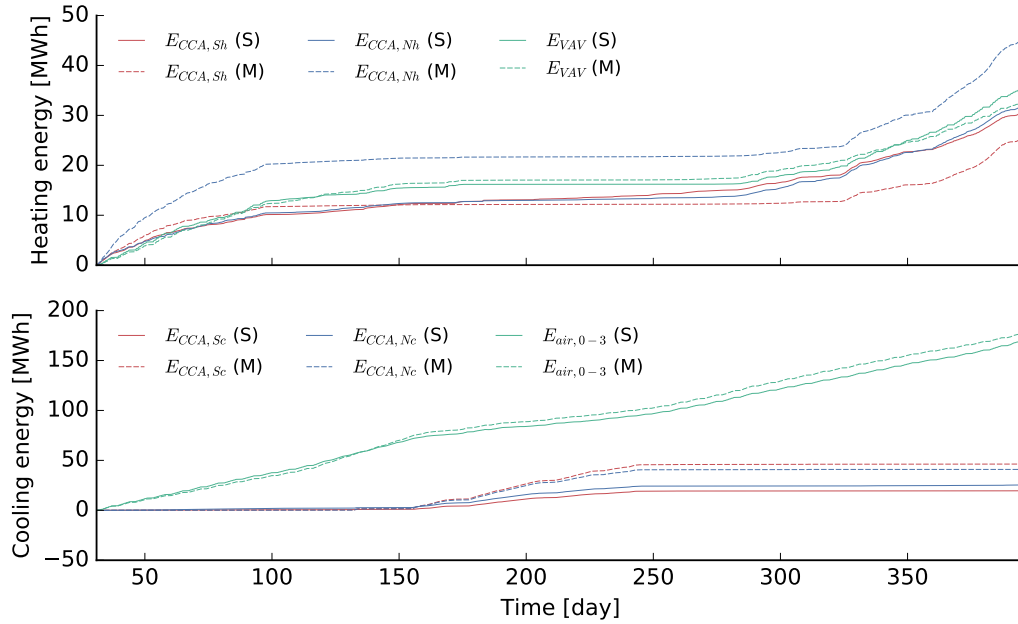Figure 15: Energy balance of the building envelope model (simulated).

Figure 16: Comparison of simulated and measured energy use.

A Landscape figures

This appendix repeats specific figures from the paper in a landscape orientation to be able to distinguish details better.
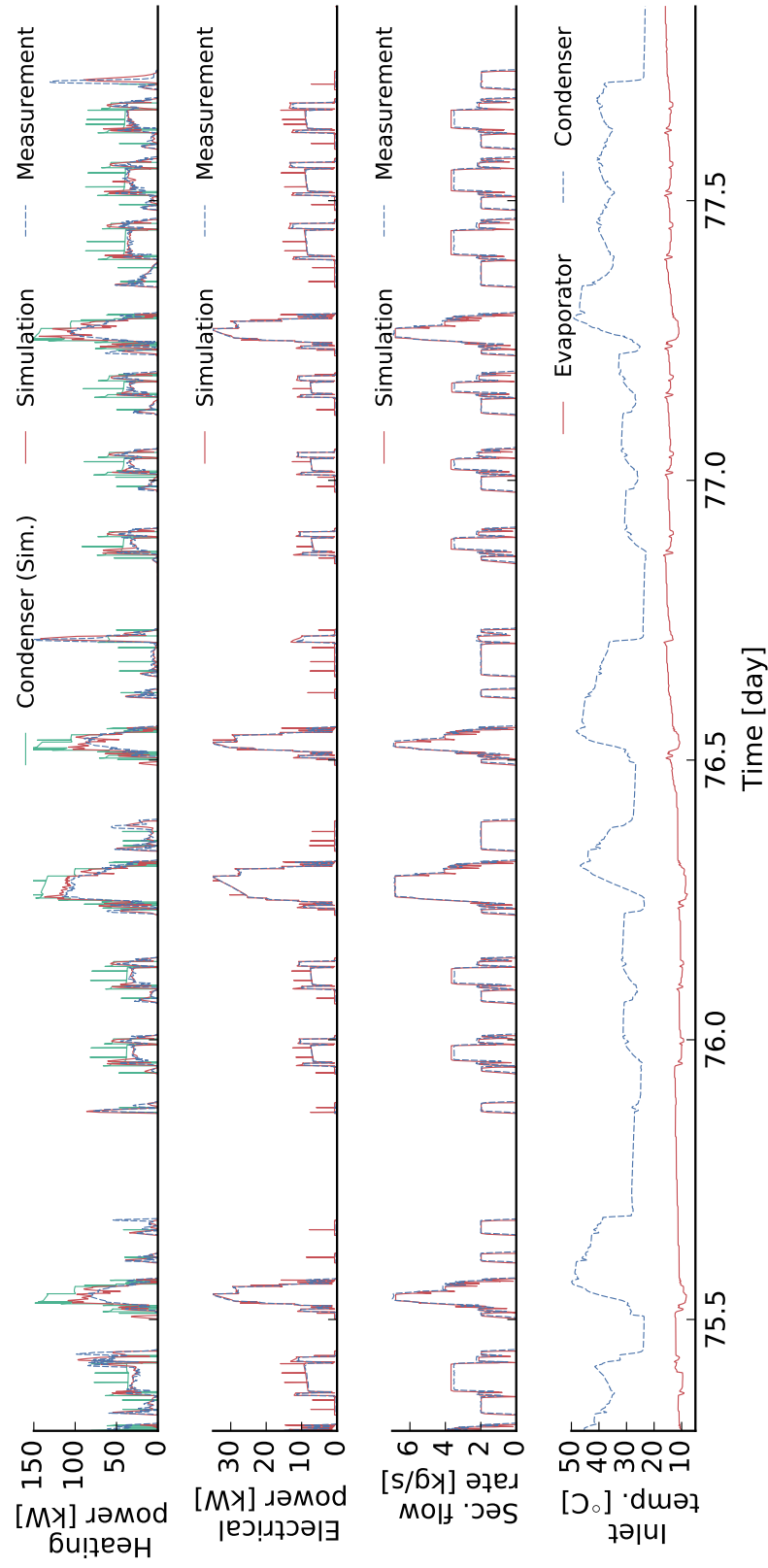
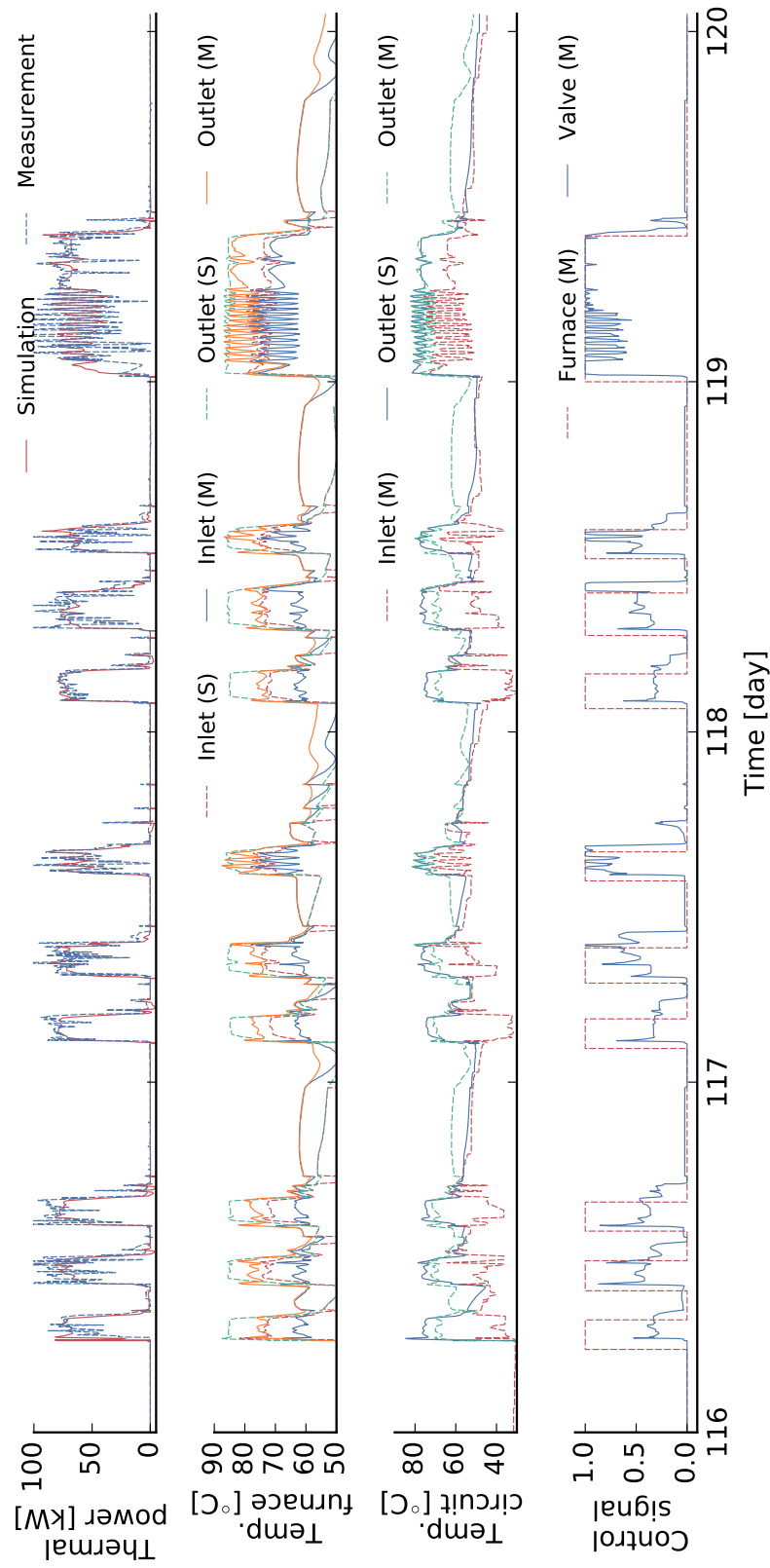Figure 17: Verification of heat pump subcircuit. Copy in landscape orientation from the paper.

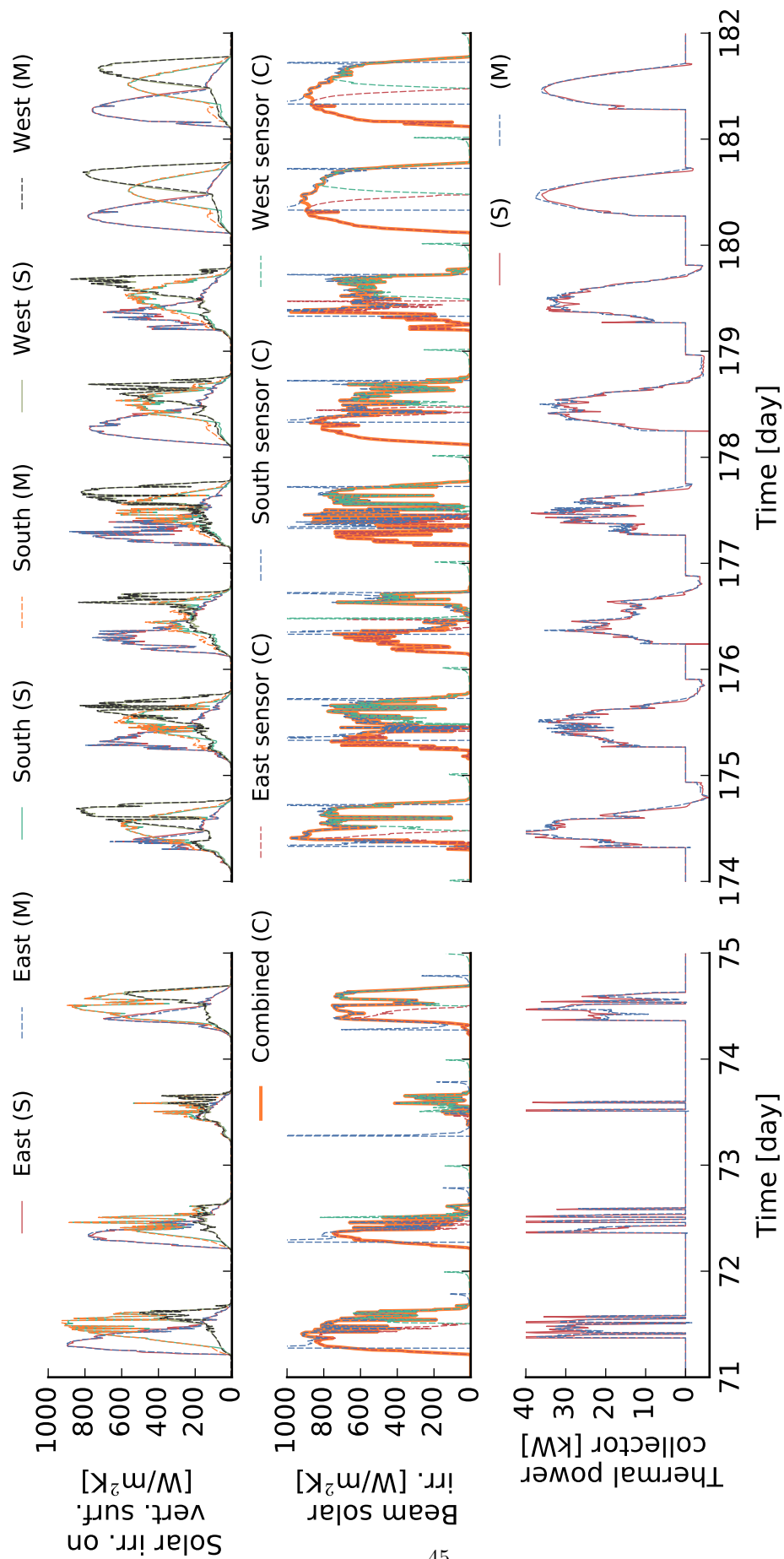Figure 18: Verification of pellet furnace subcircuit. Copy in landscape orientation from the paper.

44

Figure 19: Verification of solar collector subcircuit for a winter (left) and summer (right) period. Copy in landscape orientation from the paper.
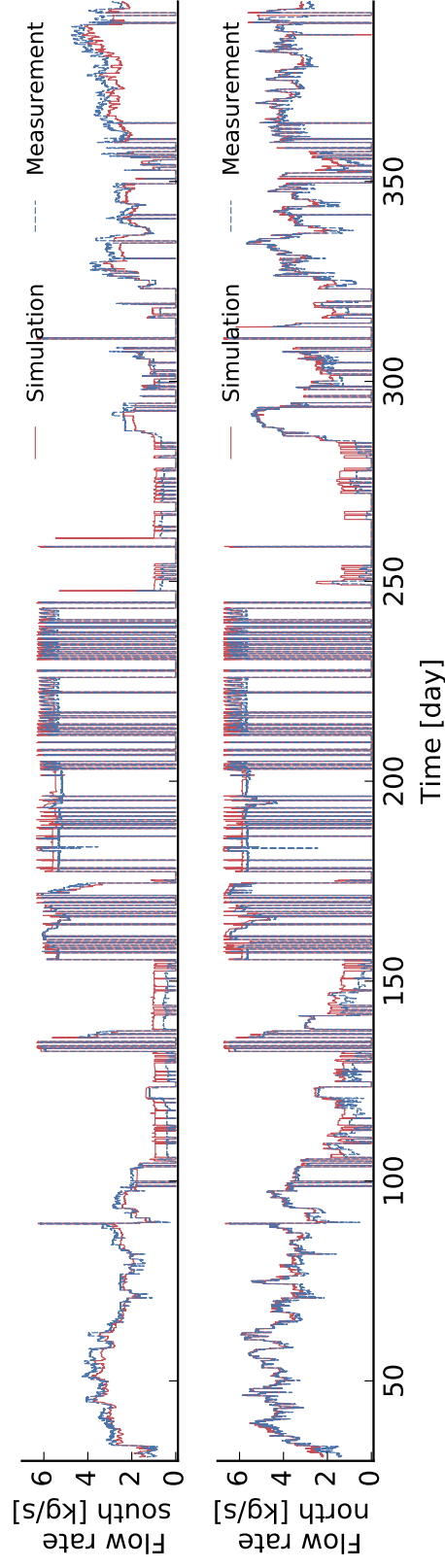
Figure 20: Comparison between measured and simulated values of total mass flow rates of north and south CCA circuits. Copy in landscape orientation from the paper.
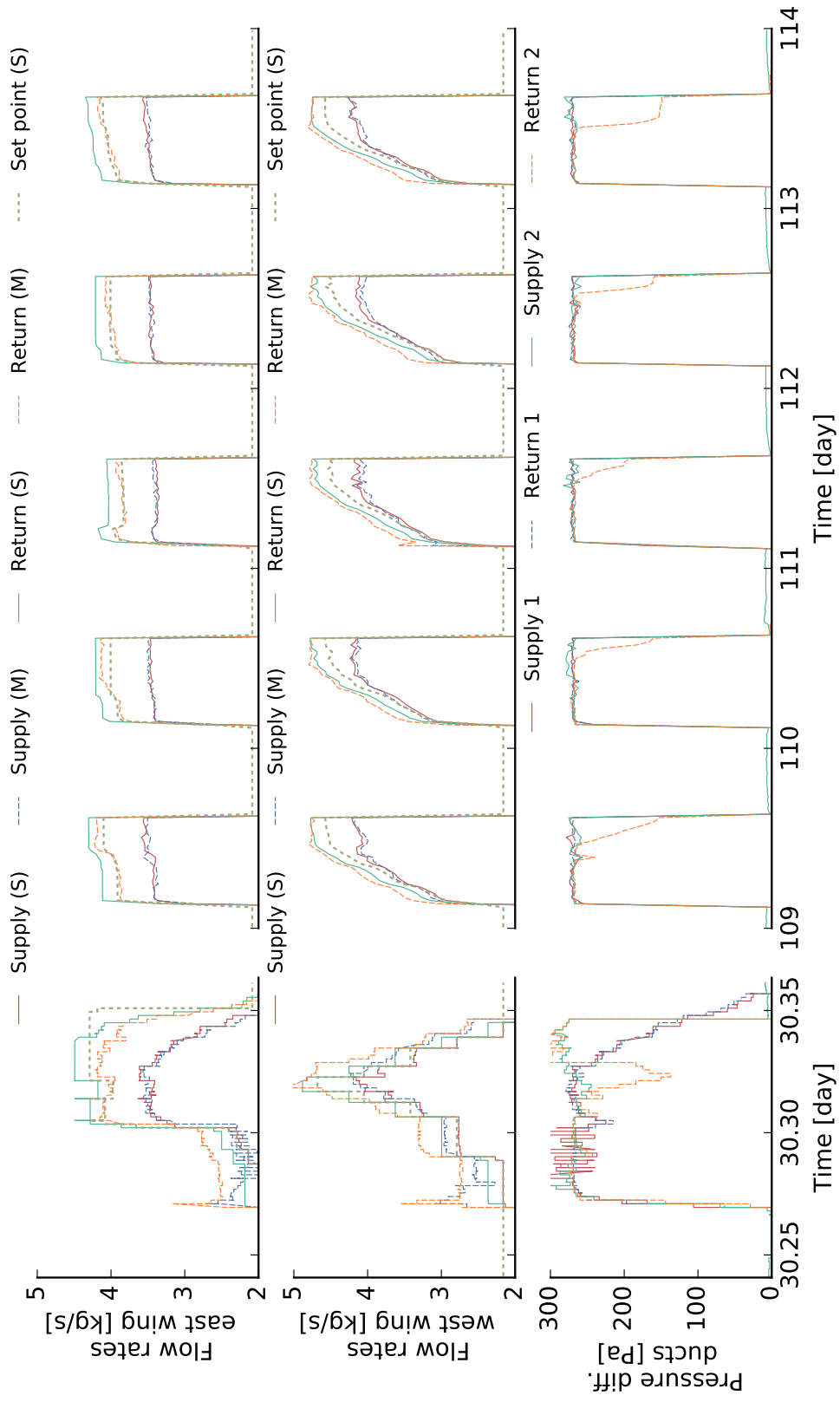
46

Figure 21: Comparison between measured and simulated values of total supply and return mass flow rates of AHU1 and AHU2. Copy in landscape orientation from the paper.
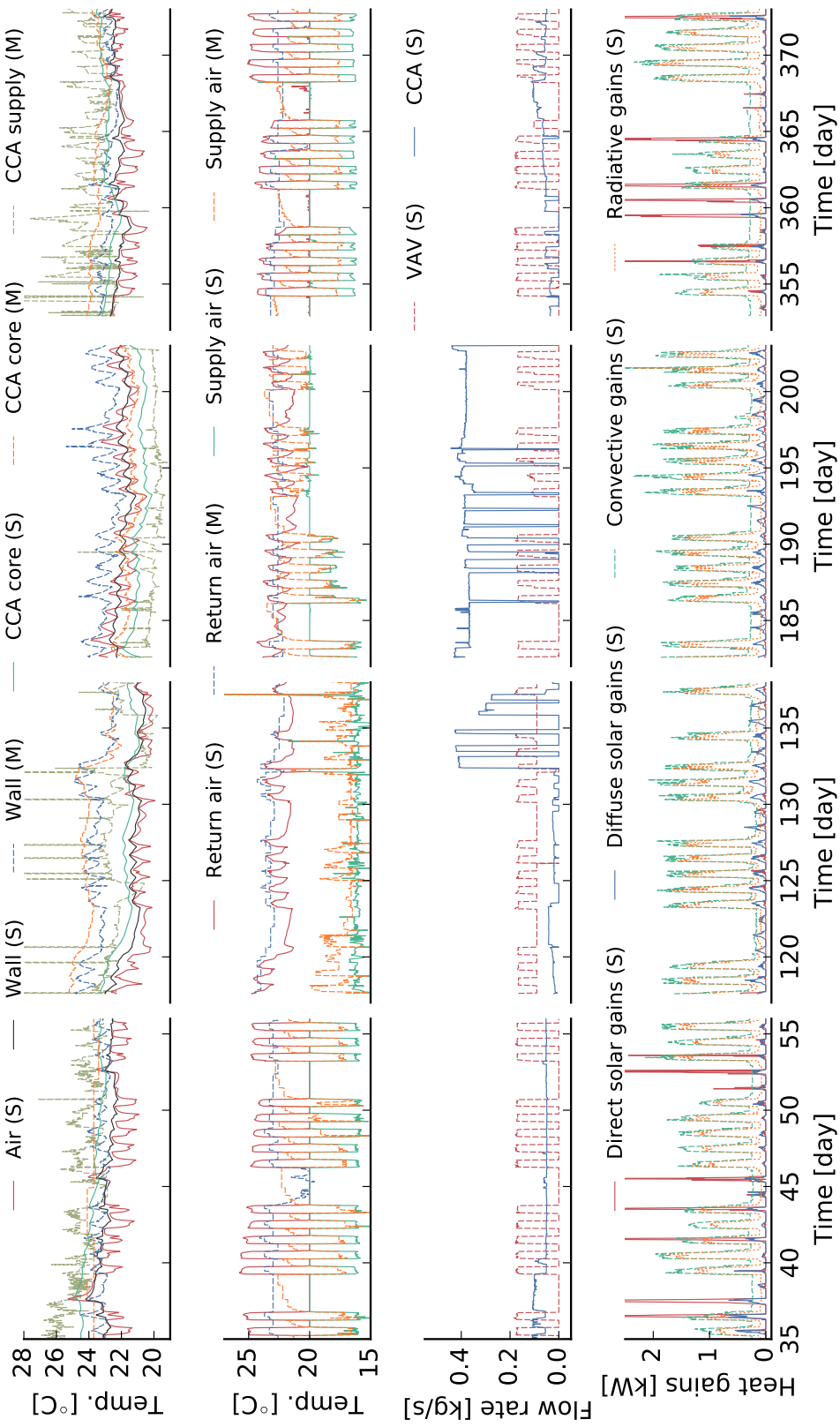
Figure 22: Verification of building envelope model using measured boundary conditions. In the top two graphs, air, concrete core and wall temperatures are compared with measurements. The bottom two graphs facilitate interpretation of the results. Two winter periods (first and fourth), a spring period (second) and a summer period (third) are shown.

References

ASHRAE. *ASHRAE handbook: Fundamentals (SI edition)*. American Society of Heating, Refrigerating and Air Conditioning Engineers, Atlanta, 2008.

H. Awbi and a. Hatton. Natural convection from heated room surfaces. *Energy & Buildings*, 30(3): 233–244, aug 1999. doi: 10.1016/S0378-7788(99)00004-3.

R. Baetens. *On externalities of heat pump-based low-energy dwellings at the low-voltage distribution grid*. PhD thesis, KU Leuven, Belgium, 2015.

R. Baetens, R. De Coninck, F. Jorissen, D. Picard, L. Helsen, and D. Saelens. OPENIDEAS - An Open Framework for Integrated District Energy Simulations. In J. Mathur and V. Garg, editors, *14th Conference of International Building Performance Simulation Association*, pages 347–354, Hyderabad, 2015. IBPSA.

T. Bergman, F. Incropera, D. DeWitt, and A. Lavine. *Fundamentals of Heat and Mass Transfer*. Wiley, 2011. ISBN 9780470501979.

E. U. Finlayson, D. K. Arasteh, C. Huizenga, M. D. Rubin, and M. S. Reilly. *Window 4.0: Documentation of Calculation Procedures*. Lawrence Berkeley Laboratory, Berkeley, 1993.

J. L. M. Hensen and M. J. H. Hamelinck. Energy Simulation of Displacement Ventilation in Offices. *Building Services Engineering Research & Technology*, 16(2):77–81, 1995. doi: 10.1177/014362449501600202.

K. G. T. Hollands, G. D. Raithby, and L. Konicek. Correlation Equations for Free Convection Heat Transfer in Horizontal Layers of Air and Water. *International Journal of Heat and Mass Transfer*, 18:879–884, 1975. ISSN 0017-9310. doi: http://dx.doi.org/10.1016/0017-9310(75)90179-9.

F. Jorissen, W. Boydens, and L. Helsen. Simulation-based occupancy estimation in office buildings using CO_2 sensors. In C. S. Barnaby and M. Wetter, editors, *15th Conference of International Building Performance Simulation Association*, pages 1073 – 1082, San Francisco, 2017. IBPSA. Paper 285.

F. Jorissen, W. Boydens, and L. Helsen. Validated air handling unit model using indirect evaporative cooling. *Journal of Building Performance Simulation*, 11(1):48–64, 2018a. doi: 10.1080/19401493.2016.1273391.

F. Jorissen, G. Reynders, R. Baetens, D. Picard, D. Saelens, and L. Helsen. Implementation and Verification of the IDEAS Building Energy Simulation Library. *Journal of Building Performance Simulation*, 11(6):669–688, 2018b. doi: 10.1080/19401493.2018.1428361.

F. Jorissen, M. Wetter, and L. Helsen. Simplifications for Hydronic System Models in Modelica. *Journal of Building Performance Simulation*, 11(6):639–654, 2018c. doi: 10.1080/19401493.2017.1421263.

W. Kays and A. London. *Compact Heat Exchangers*. McGraw-Hill, 2 edition, 1964.

M. Koschenz and B. Lehmann. *Thermoaktive Bauteilsysteme tabs*. EMPA-Akademie, Dübendorf (Switzerland), 2000.

Y. Li, M. Sandberg, and L. Fuchs. Vertical Temperature Profiles in Rooms Ventilated by Displacement: Full-Scale Measurement and Nodal Modelling. *Indoor Air*, 2(4):225–243, 1992. doi: 10.1111/j.1600-0668.1992.00005.x.

Y. Lin and P. Linden. A model for an under floor air distribution system. *Energy and Buildings*, 37(4):399 – 409, 2005. ISSN 0378-7788. doi: https://doi.org/10.1016/j.enbuild.2004.07.011. URL http://www.sciencedirect.com/science/article/pii/S0378778804002506.

N. M. Mateus and G. Carrilho da Graça. A validated three-node model for displacement ventilation. *Building and Environment*, 84:50–59, 2015. ISSN 03601323. doi: 10.1016/j.buildenv.2014.10.029. URL http://dx.doi.org/10.1016/j.buildenv.2014.10.029.

A. Meier. Infiltration: just ACH_{50} divided by 20? *Home energy*, 11(1):25–37, 1994.

A. Novoselac, B. J. Burley, and J. Srebric. Development of new and validation of existing convection correlations for rooms with displacement ventilation systems. *Energy and Buildings*, 38:163–173, 2006. ISSN 03787788. doi: 10.1016/j.enbuild.2005.04.005.

R. Perez, R. Seals, P. Ineichen, R. Stewart, and D. Menicucci. A new simplified version of the Perez diffuse irradiance model for tilted surfaces. *Solar Energy*, 39(3):221–231, 1987. ISSN 0038092X. doi: 10.1016/S0038-092X(87)80031-2.

R. Perez, P. Ineichen, R. Seals, J. Michalsky, and R. Stewart. Modeling Daylight Availability and Irradiance Components From Direct And Global Irradiance. *Solar Energy*, 44(5):271–289, 1990. doi: 10.1016/0038-092X(90)90055-H.

D. Picard and L. Helsen. Advanced Hybrid Model for Borefield Heat Exchanger Performance Evaluation, an Implementation in Modelica. In H. Tummescheit and K.-E. Arzen, editors, *10th International Modelica Conference 2014*, pages 857–866, Lund, mar 2014. Modelica Association and Linkoping University Electronic Press. doi: 10.3384/ecp14096857.

S. J. Rees and P. Haves. A nodal model for displacement ventilation and chilled ceiling systems in office spaces. *Building and Environment*, 36(6):753–762, 2001. doi: 10.1016/S0360-1323(00)00067-6.

M. Sourbron. *Dynamic thermal behaviour of buildings with concrete core activation.* PhD thesis, KU Leuven, Belgium, 2012.

U.S. Department of Energy. EnergyPlus Version 8.8 Documentation - Engineering Reference. Technical report, 2017. URL https://energyplus.net/sites/all/modules/custom/nrel_custom/pdfs/pdfs_v8.8.0/EngineeringReference.pdf. [Online; visited 17 December 2017].

T. Webster, F. Bauman, M. Shi, and J. Reese. Thermal stratification performance of underfloor air distribution (UFAD) systems. In *Indoor Air 2002*, Monterey, CA, 2002.

M. Wetter. Fan and pump model that has a unique solution for any pressure boundary condition and control signal. In *13-th Conference of International Building Performance Simulation Association*, pages 3505–3512, Chambéry, 2013. IBPSA.

M. Wetter, M. Fuchs, P. Grozman, L. Helsen, F. Jorissen, M. Lauster, M. Dirk, C. Nytsch-geusen, D. Picard, P. Sahlin, and M. Thorade. IEA EBC Annex 60 Modelica Library - An International Collaboration to Develop a Free Open-Source Model Library for Buildings and Community Energy Systems. In J. Mathur and V. Garg, editors, *14th Conference of International Building Performance Simulation Association*, pages 395–402, Hyderabad, 2015. International Building Performance Simulation Association.

X. Wu, B. W. Olesen, L. Fang, and J. Zhao. A nodal model to predict vertical temperature distribution in a room with floor heating and displacement ventilation. *Building and Environment*, 59:626–634, 2013. doi: 10.1016/j.buildenv.2012.10.002.